Journal of Marine Research, 67, 1–36, 2009

A shallow water model conserving energy and potential enstrophy in the presence of boundaries

by Rick Salmon[1]

ABSTRACT

We extend a previously developed method for constructing shallow water models that conserve energy and potential enstrophy to the case of flow bounded by rigid walls. This allows the method to be applied to ocean models. Our procedure splits the dynamics into a set of prognostic equations for variables (vorticity, divergence, and depth) chosen for their relation to the Casimir invariants of mass, circulation and potential enstrophy, and a set of diagnostic equations for variables that are the functional derivatives of the Hamiltonian with respect to the chosen prognostic variables. The form of the energy determines the form of the diagnostic equations. Our emphasis on conservation laws produces a novel form of the boundary conditions, but numerical test cases demonstrate the accuracy of our model and its extreme robustness, even in the case of vanishing viscosity.

1. Introduction

A previous paper (Salmon, 2007, hereafter S07) offered a general method for constructing energy- and potential-enstrophy-conserving models of the shallow water equations in domains of arbitrary shape. Although explicit results were shown only for the case of flow on the periodic plane, S07 also derived the evolution equations for the case of an arbitrary, unstructured triangular mesh. S07 further claimed that the new methods generalize to the case of flows bounded by solid walls, but the precise method for incorporating solid boundaries was not described.

The present paper has two purposes. The first purpose is to explain the procedure for incorporating solid boundaries in complete detail. This allows the method to be applied to ocean models, in which boundary conditions are always important. The second purpose is to reprise the entire method with less explicit reference to the Hamiltonian tools used so extensively in S07. Although the clear separation of shallow water dynamics into its two Hamiltonian constituents—the Poisson bracket and the Hamiltonian—still guides the construction of the numerical algorithm, the present paper avoids Nambu brackets. Because the incorporation of boundary conditions into Poisson brackets is problematic, the less

1. Scripps Institution of Oceanography, University of California, La Jolla, California, 92093, U.S.A. ***email: rsalmon@ucsd.edu***

Hamiltonian flavor of the present approach seems to be a positive advantage when considering flows within rigid boundaries. In any case, the greater directness and generality of the present derivations might appeal to a broader range of users, and should extend more readily to other applications.

The first—and still the simplest—energy and potential-enstrophy conserving shallow-water scheme is that derived by Arakawa and Lamb (1981, hereafter AL). The AL scheme uses the velocity components u and v, and the fluid depth h as the fundamental dynamical variables, and it does not require the solution of elliptic equations. In contrast, the method of S07 uses the vorticity ζ, the divergence μ, and the depth h as fundamental variables, and it requires the solution of coupled elliptic equations to determine the streamfunction and velocity potential at every time step. The need to solve elliptic equations makes the S07 method less efficient than the AL method. However, AL has proved difficult to generalize to arbitrary geometry, and a method for incorporating rigid boundary conditions into AL has only recently been described by Ketefian and Jacobson (2009). Furthermore, as noted in S07, the AL algorithm distorts the dispersion relation for inertia-gravity waves unless the Rossby deformation radius is much larger than the grid spacing. Thus, despite its relative inefficiency, the method of S07 offers definite advantages over AL.

Of course, no matter what the method, eddy viscosity must be present to compensate for the finite spatial resolution of the model. However, the form of the eddy viscosity, and especially its accompanying boundary conditions, are quite arbitrary. The ideal shallow water equations with their conservation properties are grounded in physics, but the eddy viscosity is a matter of choice and necessity. For this reason, we separate the complete dynamics into two parts—an ideal, inviscid part, and a part that corresponds to the eddy viscosity—and we construct our model in such a way that the two parts can either be separately advanced or solved together by a Strang splitting of the time step. In any case, this paper is primarily concerned with the construction of the ideal, inviscid part of the model.

The argument is sometimes made that conservation laws don't matter if eddy viscosity is present, because the viscosity destroys them. This argument misses the point. If the ideal, inviscid part of the dynamics did not conserve energy (for example), then the system would contain a spurious *internal* source of energy. At the very least, this internal source would invalidate any attempt to infer an energy budget from the computations. However, it seems possible that some computer codes rely on viscosity to control numerical instabilities that occur only because the ideal part of the dynamics is poorly designed. Maintaining conservation laws could prevent such numerical instabilities.

The plan of the paper is as follows. Section 2 outlines the general approach, emphasizing the clear separation between the prognostic equations, which correspond to the Poisson bracket of the shallow water equations, and the diagnostic equations, which correspond to the Hamiltonian. Section 3 derives the complete set of finite-difference equations for the case of a rectangular domain with solid boundaries. Section 4 considers the special case of rotating flow in a channel, in which nothing varies in the along-channel direction. The derivation

of the finite-difference equations is simpler and more illuminating in this one-dimensional case, and one sees clearly how the insistence upon conservation laws automatically produces a consistent set of boundary conditions. Section 4 tests these somewhat unconventional boundary conditions by comparing solutions of the one-dimensional model to the solutions of a Lagrangian model, in which the boundary conditions and most of the conservation laws are built into the formulation. The solutions agree closely despite huge differences in the way the two models are constructed. Section 5 presents two-dimensional solutions, with and without viscosity, in a square ocean basin with a variable Coriolis parameter and an equator at mid-basin. Section 6 concludes with an assessment of the method and its potential for further generalization.

2. General method

The shallow water equations may be written in the form

$$\frac{\partial u}{\partial t} = qvh - \frac{\partial \Phi}{\partial x} \tag{2.1a}$$

$$\frac{\partial v}{\partial t} = -quh - \frac{\partial \Phi}{\partial y} \tag{2.1b}$$

$$\frac{\partial h}{\partial t} + \frac{\partial}{\partial x}(uh) + \frac{\partial}{\partial y}(vh) = 0 \tag{2.1c}$$

where (u, v) is the horizontal velocity in the (x, y) direction at time t, h is the fluid depth,

$$q = (\zeta + f)/h \tag{2.2}$$

is the potential vorticity with relative vorticity ζ and Coriolis parameter f, and

$$\Phi = \frac{1}{2}(u^2 + v^2) + gh. \tag{2.3}$$

At solid boundaries, both the normal component of velocity and its time derivative must vanish. Hence

$$\mathbf{u} \cdot \mathbf{n} = 0 \tag{2.4a}$$

$$qh\, \mathbf{u} \cdot \mathbf{s} - \frac{\partial \Phi}{\partial n} = 0 \tag{2.4b}$$

at solid boundaries. Here, $\mathbf{u} = (u, v)$; and n and s are the outward-normal and counter-clockwise-tangent unit vectors, respectively.

The AL scheme is based upon the shallow water equations in the form (2.1). However, as explained in S07, it is easier to construct Casimir-conserving schemes if the fundamental dynamical variables u and v are replaced by the vorticity $\zeta = v_x - u_y$ and the divergence

$\mu = u_x + v_y$, where the subscripts denote partial derivatives. The conserved Casimirs include the mass,

$$\iint d\mathbf{x}\, h \tag{2.5a}$$

the circulation,

$$\iint d\mathbf{x}\, hq \tag{2.5b}$$

and the potential enstrophy,

$$\iint d\mathbf{x}\, hq^2. \tag{2.5c}$$

In terms of the new variables, the evolution equations take the forms

$$\frac{\partial \zeta}{\partial t} = J(q, \chi) - \nabla \cdot (q \nabla \gamma) \tag{2.6a}$$

$$\frac{\partial \mu}{\partial t} = J(q, \gamma) + \nabla \cdot (q \nabla \chi - \nabla \Phi) \tag{2.6b}$$

$$\frac{\partial h}{\partial t} = -\nabla^2 \gamma \tag{2.6c}$$

where $J(R, S) \equiv R_x S_y - S_x R_y$ is the Jacobian operator, and $\nabla F \equiv (F_x, F_y)$. The streamfunction χ and the velocity potential γ are defined by

$$h\mathbf{u} = \left(-\frac{\partial \chi}{\partial y} + \frac{\partial \gamma}{\partial x}, \ \frac{\partial \chi}{\partial x} + \frac{\partial \gamma}{\partial y} \right) \tag{2.7}$$

and are determined from ζ, μ, h by the elliptic equations

$$\nabla \cdot (h^{-1} \nabla \chi) + J(h^{-1}, \gamma) = \zeta \tag{2.8a}$$

$$\nabla \cdot (h^{-1} \nabla \gamma) + J(\chi, h^{-1}) = \mu \tag{2.8b}$$

and boundary conditions equivalent to (2.4). Although (2.4a) implies only the *single* condition $-\chi_s + \gamma_n = 0$ on the *two* variables χ and γ, we shall require the two boundary conditions

$$\chi = 0 \tag{2.9a}$$

$$\partial \gamma / \partial n = 0 \tag{2.9b}$$

which remove a physically irrelevant arbitrariness in the values of χ and γ. Eqs. (2.9) determine χ uniquely, and γ to within a physically irrelevant constant. The boundary condition (2.4b) becomes

$$q \left(\frac{\partial \gamma}{\partial s} + \frac{\partial \chi}{\partial n} \right) - \frac{\partial \Phi}{\partial n} = 0 \tag{2.10}$$

and the definition (2.3) becomes

$$\Phi = \frac{1}{2h^2}(\nabla\chi\cdot\nabla\chi + \nabla\gamma\cdot\nabla\gamma + 2J(\chi,\gamma)) + gh. \tag{2.11}$$

As shown in S07, the evolution equations (2.6) correspond to the general Hamiltonian equation $dF/dt = \{F, H\}$ where F is an arbitrary functional, $\{\ ,\ \}$ is the Poisson bracket, and H is the Hamiltonian—the energy—of the system. From the Hamiltonian perspective, we obtain (2.6) by taking $F = \zeta, \mu, h$ and using the shallow-water energy (2.25) for the Hamiltonian. The variables χ, γ and Φ defined by (2.7) and (2.11) turn out to be the functional derivatives (2.24) of the Hamiltonian (2.25).

In general Hamiltonian theory, a Casimir is any functional K for which $\{K, M\} = 0$ for arbitrary functional M. Thus Casimirs are conserved for arbitrary choices of the Hamiltonian H. For a general introduction to Hamiltonian fluid mechanics, see for example Salmon (1998). However, for present purposes it is sufficient to note that the evolution equations (2.6) conserve (2.5) no matter how χ, γ, and Φ are defined in terms of ζ, μ, and h. On the other hand, energy conservation depends critically on these definitions; the elliptic equations (2.8) and the definition (2.11) correspond to the choice of (2.25) as Hamiltonian. A clear distinction between these two parts of the dynamics—the evolution equations (2.6) with their Casimir-conserving properties and the diagnostic equations (2.8) and (2.11) with their implications for energy conservation—is key to the construction of numerical algorithms that maintain the conservation laws.

Our first task is to discretize the evolution equations (2.6). Complete details will be given in Section 3; in this section, we present the outline of the method. For simplicity, we consider a rectangular domain covered by a square mesh. The generalization to arbitrary domains will be obvious. We imagine the evolution equations (2.6) to hold at all points, including boundary points. Then (2.6a) is equivalent to the statement that

$$\iint d\mathbf{x}\, A\frac{\partial\zeta}{\partial t} = \iint d\mathbf{x}[AJ(q,\chi) - A\nabla\cdot(q\nabla\gamma)] \tag{2.12}$$

for arbitrary function $A(x, y)$. Using the boundary conditions (2.9), we write (2.12) in the form

$$\iint d\mathbf{x}\, A\frac{\partial\zeta}{\partial t} = \iint d\mathbf{x}\left[\frac{1}{3}AJ(q,\chi) + \frac{1}{3}qJ(\chi,A) + \frac{1}{3}\chi J(A,q) + q\nabla\gamma\cdot\nabla A\right]. \tag{2.13a}$$

Similarly, (2.6b) is equivalent to

$$\iint d\mathbf{x}\, B\frac{\partial\mu}{\partial t} = \iint d\mathbf{x}\,[qJ(\gamma,B) - q\nabla\chi\cdot\nabla B + \nabla\Phi\cdot\nabla B] \tag{2.13b}$$

and (2.6c) is equivalent to

$$\iint d\mathbf{x}\, C\frac{\partial h}{\partial t} = \iint d\mathbf{x}[\nabla C\cdot\nabla\gamma] \tag{2.13c}$$

where $B(x, y)$ and $C(x, y)$ are arbitrary functions. In writing (2.13b) we make use of (2.10), and in writing (2.13c) we use (2.9b) again. These are the only explicit uses of the boundary conditions that we shall require. Note that the Jacobian term in (2.13a) has been split into 3 pieces, whereas the Jacobian term in (2.13b) has not. The reason for this unequal treatment will presently be clear, but here we note that it corresponds to the unequal treatment of (3.2) and (3.6) in S07. Summing (2.13) we obtain

$$\iint d\mathbf{x} A\frac{\partial \zeta}{\partial t} + B\frac{\partial \mu}{\partial t} + C\frac{\partial h}{\partial t} = \iint d\mathbf{x}\left[\frac{1}{3}AJ(q, \chi) + \frac{1}{3}qJ(\chi, A) + \frac{1}{3}\chi J(A, q)\right.$$
$$\left. + qJ(\gamma, B) + q\nabla\gamma\cdot\nabla A - q\nabla\chi\cdot\nabla B + \nabla\Phi\cdot\nabla B + \nabla C\cdot\nabla\gamma\right]. \quad (2.14)$$

The evolution equations (2.6) are equivalent to the statement that (2.14) holds for arbitrary functions A, B, and C. Conservation of the Casimirs (2.5) corresponds to particular choices of these 'test functions', namely

$$A = B = 0, \quad C = 1 \quad \text{(mass)} \quad (2.15a)$$
$$A = 1, \quad B = C = 0 \quad \text{(circulation)} \quad (2.15b)$$
$$A = 2q, \quad B = 0 \quad C = -q^2 \quad \text{(potential enstrophy)}. \quad (2.15c)$$

For example, to establish conservation of potential enstrophy, we substitute (2.15c) into (2.14) to obtain

$$\iint d\mathbf{x}\left[2q\frac{\partial \zeta}{\partial t} - q^2\frac{\partial h}{\partial t}\right]$$
$$= \iint d\mathbf{x}\left[\frac{1}{3}2qJ(q, \chi) + \frac{1}{3}qJ(\chi, 2q) + \frac{1}{3}\chi J(2q, q) + q\nabla\gamma\cdot 2\nabla q - \nabla q^2\cdot\nabla\gamma\right]. \quad (2.16)$$

The rhs of (2.16) vanishes, and the lhs is the time-derivative of (2.5c).

We obtain Casimir-conserving, finite-difference analogs of (2.6) by discretizing (2.14) in such a way that cancellations like those in (2.16) are maintained by the finite-difference forms. It was the need to maintain these cancellations that motivated the parts-integrations in (2.13). In particular, as first noted by Salmon and Talley (1989), the splitting of the single Jacobian term in (2.12) into the *three* terms in (2.13a) means that the three Jacobian terms in the finite-difference analog of (2.16) will cancel provided only that the finite-difference Jacobian maintains the antisymmetry property $J(F, G) = -J(G, F)$ of the exact Jacobian. This antisymmetry property is very easy to maintain. The cancellation between the finite-difference forms of the last two terms in (2.16) is only slightly more subtle. Cancellation occurs if the first of these terms takes the general finite-difference form

$$\frac{1}{2}(q_i + q_{i+1})(\gamma_{i+1} - \gamma_i)2(q_{i+1} - q_i) \quad (2.17)$$

(in one or more directions) and if the last term in (2.16) takes the finite-difference form

$$-\left(q_{i+1}^2 - q_i^2\right)(\gamma_{i+1} - \gamma_i). \tag{2.18}$$

The sum of (2.17) and (2.18) vanishes. The following section provides more details.

Strictly speaking, the vanishing of the finite-difference form of the rhs of (2.16) is a necessary but insufficient condition for the conservation of a finite-difference form of potential enstrophy. It must also be true that the finite-difference approximation to the lhs of (2.16) is an exact time derivative. In practice, this is very easy to arrange, because the fundamental variables ζ and h are so closely related to the Casimirs. For example, if the lhs of (2.14) is approximated as

$$\sum_{ij} A_{ij}\frac{d\zeta_{ij}}{dt} + B_{ij}\frac{d\mu_{ij}}{dt} + C_{ij}\frac{dh_{ij}}{dt} \tag{2.19}$$

where the sum is over all grid points, then the lhs of (2.16) is

$$\sum_{ij} 2q_{ij}\frac{d\zeta_{ij}}{dt} - q_{ij}^2\frac{dh_{ij}}{dt} \tag{2.20}$$

and is equal to

$$\frac{d}{dt}\sum_{ij} h_{ij}q_{ij}^2 \tag{2.21}$$

provided only that $q_{ij} = (\zeta_{ij} + f)/h_{ij}$. Here, as in S07, we regard the time derivatives as exact. That is, we ignore the truncation error associated with the discretization of the time derivative. Long experience, and the numerical experiments described in Section 5, show that this error is negligible in comparison with the truncation error associated with the discretization of the space derivatives.

In summary, our method conserves analogs of the three Casimirs (2.5) for *arbitrary* gridded values of χ, γ, and Φ. The arbitrariness of χ, γ, Φ corresponds to the property that the Casimirs depend only on the form of the Poisson bracket, and are conserved for arbitrary values of the Hamiltonian. The specific choice of χ, γ, Φ corresponds to the specific choice of the Hamiltonian, that is, to a specific expression for the conserved energy.

From the standpoint of (2.14) energy conservation corresponds to

$$A = -\chi, \quad B = -\gamma \quad C = \Phi \quad \text{(energy)}. \tag{2.22}$$

Once again, the rhs cancellations are easily maintained by finite-difference approximations; it is only necessary that the Jacobian terms in (2.13a) and the gradient terms in (2.13a,b,c) be discretized in the same way. The finite-difference approximation to the Jacobian in (2.13b) need only have the property of antisymmetry; it must vanish when $B = \gamma$. In particular, the

form of this Jacobian need not be related to the finite-difference form of the Jacobians in (2.13a). However, energy conservation also requires that the finite-difference analog of the lhs of

$$\iint d\mathbf{x}\left[-\chi\frac{\partial\zeta}{\partial t}-\gamma\frac{\partial\mu}{\partial t}+\Phi\frac{\partial h}{\partial t}\right]=0 \tag{2.23}$$

be an exact time derivative. This is a nontrivial requirement. As shown in S07,

$$\chi=-\frac{\delta H}{\delta\zeta},\quad \gamma=-\frac{\delta H}{\delta\mu},\quad \Phi=\frac{\delta H}{\delta h} \tag{2.24}$$

are the functional derivatives of the Hamiltonian. By the chain rule for functional derivatives, (2.23) and (2.24) imply conservation of energy, $dH/dt=0$. Thus (2.24) and the choice of Hamiltonian determines the link between the 'diagnostic' variables χ, γ, and Φ, and the 'prognostic' variables ζ, μ and h. The specific choice

$$\begin{aligned}H&=\iint\left(\frac{1}{2}h\,\mathbf{u}\cdot\mathbf{u}+\frac{1}{2}gh^2\right)\\&=\iint\left(\frac{1}{2h}(\nabla\chi\cdot\nabla\chi+\nabla\gamma\cdot\nabla\gamma+2J(\chi,\gamma))+\frac{1}{2}gh^2\right)\end{aligned} \tag{2.25}$$

corresponds to the elliptic equations (2.8) and to the definition (2.11) of Φ.

The following section provides full details, but the general strategy of our procedure should already be clear: Instead of the customary variables $\{u, v, h\}$, we adopt a set of prognostic variables $\{\zeta, \mu, h\}$ and a set of diagnostic variables $\{\chi, \gamma, \Phi\}$. The prognostic variables are chosen for their simple relationship to the Casimirs (2.5); the diagnostic variables are the functional derivatives of the Hamiltonian (2.25) with respect to the chosen prognostic variables. The evolution equations for the prognostic variables must be discretized in such a way that the Casimirs are conserved for *arbitrary* values of the diagnostic variables. Then conservation of energy determines the discrete form of the diagnostic equations. Although some understanding of Hamiltonian fluid mechanics is helpful, it is certainly seems possible to follow this recipe without it.

3. Domain covered by square grid boxes

We consider a bounded fluid domain covered by square grid boxes. For simplicity, we take the fluid domain to be a rectangle, but our results generalize easily. For the case of a rectangular domain, every grid box falls into one of three categories: interior grid boxes not touching boundaries, grid boxes touching boundaries but not at corners, and corner grid boxes. We replace (2.14) by the finite-difference form

$$\sum_{\text{gridpoints}} w_{ij}\left[A_{ij}\frac{d\zeta_{ij}}{dt}+B_{ij}\frac{d\mu_{ij}}{dt}+C_{ij}\frac{dh_{ij}}{dt}\right]$$
$$=\sum_{\text{gridboxes}}\left[\frac{1}{3}[A,q,\chi]+\frac{1}{3}[q,\chi,A]+\frac{1}{3}[\chi,A,q]\right.$$
$$\left.+[q,\gamma,B]+(q,\gamma,A)-(q,\chi,B)+(B,\Phi)+(C,\gamma)\right]. \tag{3.1}$$

On the lhs of (3.1), the sum is over grid points (i, j) located at $(x, y) = (i\Delta, j\Delta)$, where Δ is the grid spacing. Each grid point receives a weight w_{ij} proportional to its contribution to the total area. For interior grid points $w_{ij} = 1$; for boundary grid points not at corners $w_{ij} = 1/2$; and for corner grid points $w_{ij} = 1/4$. The rhs of (3.1) is a summation over grid boxes. All the grid boxes have the same size and receive the same weight. On each grid box,

$$[A,B,C]=\frac{1}{8\Delta^2}(A_a+A_b+A_c+A_d)\times[(B_c-B_a)(C_d-C_b)-(C_c-C_a)(B_d-B_b)] \tag{3.2}$$

is the finite-difference approximation to $\iint d\mathrm{x}\; AJ(B,C)$;

$$(A,B,C)=\frac{1}{4\Delta^2}[(A_a+A_b)(B_b-B_a)(C_b-C_a)+(A_b+A_c)(B_c-B_b)(C_c-C_b)$$
$$+(A_c+A_d)(B_d-B_c)(C_d-C_c)+(A_d+A_a)(B_a-B_d)(C_a-C_d)] \tag{3.3}$$

approximates $\iint d\mathbf{x}\; A\nabla B\cdot\nabla C$; and

$$(A,B)=\frac{1}{2\Delta^2}[(A_b-A_a)(B_b-B_a)+(A_c-A_b)(B_c-B_b)$$
$$+(A_d-A_c)(B_d-B_c)+(A_a-A_d)(B_a-B_d)] \tag{3.4}$$

approximates $\iint\; d\mathbf{x}\;\nabla A\cdot\nabla B$. The subscripts in (3.2-3.4) refer to the representative grid box shown in Figure 1. As regards (3.2-3.4), it makes no difference whether the grid box lies in the interior or along a boundary. **Figure 1**

We obtain the evolution equation for ζ_{ij} by taking the A_{ij}-derivative of (3.1), and similarly for μ_{ij} and h_{ij}. If (i, j) is an interior grid point, then four grid boxes contribute to each evolution equation, and the evolution equations are identical to (3.15) in S07. These equations appear as (A.1) in Appendix A, which collects all the final results. If (i, j) is a non-corner boundary grid point, then two grid boxes contribute to each evolution equation; representative equations are given as (A.2). If (i, j) is a corner point, then only one grid box contributes to each evolution equation; representative equations are given as (A.3). Eqs. (A.2-3) incorporate the condition $\chi_{ij} = 0$ at boundary grid points.

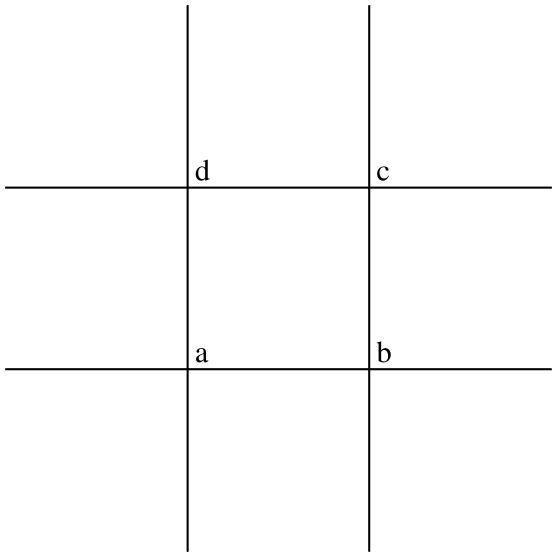

Figure 1. A representative grid box with corners identified by letters.

Given $\zeta_{ij}, \mu_{ij}, h_{ij}, \chi_{ij}, \gamma_{ij}, \Phi_{ij}$ at every grid point at some initial time, we use (A.1-3) to advance $\zeta_{ij}, \mu_{ij}, h_{ij}$ to a new time. This 'Poisson bracket' part of the dynamics conserves the mass, circulation, and potential enstrophy in the forms

$$\sum_{ij} w_{ij} h_{ij}, \quad \sum_{ij} w_{ij} h_{ij} q_{ij}, \quad \sum_{ij} w_{ij} h_{ij} q_{ij}^2. \tag{3.5}$$

To continue the process, we must determine $\chi_{ij}, \gamma_{ij}, \Phi_{ij}$ from $\zeta_{ij}, \mu_{ij}, h_{ij}$ at the new time. This involves the 'Hamiltonian' part of the dynamics.

Substitutions analogous to (2.22) lead to the analog

$$\sum_{ij} w_{ij} \left[-\chi_{ij} \frac{d\zeta_{ij}}{dt} - \gamma_{ij} \frac{d\mu_{ij}}{dt} + \Phi_{ij} \frac{dh_{ij}}{dt} \right] = 0 \tag{3.6}$$

of (2.23). The lhs of (3.6) should be the time derivative of the energy. For the energy (2.25), we choose the finite difference form

$$H = K + \sum_{\text{gridboxes}} \frac{1}{2} g \frac{\left(h_a^2 + h_b^2 + h_c^2 + h_d^2\right)}{4} \tag{3.7}$$

where

$$K = \frac{1}{2\Delta^2}\sum_{\text{gridboxes}} \frac{(\chi_b-\chi_a)^2}{(h_a+h_b)} + \frac{(\gamma_b-\gamma_a)^2}{(h_a+h_b)} + \frac{(\chi_c-\chi_b)^2}{(h_b+h_c)} + \frac{(\gamma_c-\gamma_b)^2}{(h_b+h_c)}$$
$$+ \frac{(\chi_d-\chi_c)^2}{(h_c+h_d)} + \frac{(\gamma_d-\gamma_c)^2}{(h_c+h_d)} + \frac{(\chi_a-\chi_d)^2}{(h_a+h_d)} + \frac{(\gamma_a-\gamma_d)^2}{(h_a+h_d)}$$
$$+ \frac{4[(\chi_c-\chi_a)(\gamma_d-\gamma_b)-(\gamma_c-\gamma_a)(\chi_d-\chi_b)]}{(h_a+h_b+h_c+h_d)} \tag{3.8}$$

is the finite-difference approximation to the kinetic energy in (2.25). Once again, the subscripts in (3.7-3.8) refer to Figure 1. Taking the differential of (3.7-3.8) and collecting terms, we obtain, after considerable manipulation,

$$dH = \sum_{\text{gridboxes}} -\chi_a d\zeta_a - \chi_b d\zeta_b - \chi_c d\zeta_c - \chi_d d\zeta_d - \gamma_a d\mu_a - \gamma_b d\mu_b$$
$$- \gamma_c d\mu_c - \gamma_d d\mu_d + \Phi_a dh_a + \Phi_b dh_b + \Phi_c dh_c + \Phi_d dh_d \tag{3.9}$$

where

$$\zeta_a = \frac{1}{\Delta^2}\left(\frac{(\chi_b-\chi_a)}{(h_a+h_b)} + \frac{(\chi_d-\chi_a)}{(h_a+h_d)} + \frac{2(\gamma_d-\gamma_b)}{(h_a+h_b+h_c+h_d)}\right). \tag{3.10}$$

The corresponding expressions for $\zeta_b, \zeta_c, \zeta_d$ are obtained by cyclic permutation of the subscripts. For example,

$$\zeta_b = \frac{1}{\Delta^2}\left(\frac{(\chi_c-\chi_b)}{(h_b+h_c)} + \frac{(\chi_a-\chi_b)}{(h_a+h_b)} + \frac{2(\gamma_a-\gamma_c)}{(h_a+h_b+h_c+h_d)}\right). \tag{3.11}$$

Similarly

$$\mu_a = \frac{1}{\Delta^2}\left(\frac{(\gamma_b-\gamma_a)}{(h_a+h_b)} + \frac{(\gamma_d-\gamma_a)}{(h_a+h_d)} + \frac{2(\chi_b-\chi_d)}{(h_a+h_b+h_c+h_d)}\right) \tag{3.12}$$

and

$$\Phi_a = \frac{1}{4}gh_a + \frac{1}{2\Delta^2}\left(\frac{(\chi_b-\chi_a)^2}{(h_a+h_b)^2} + \frac{(\gamma_b-\gamma_a)^2}{(h_a+h_b)^2} + \frac{(\chi_d-\chi_a)^2}{(h_a+h_d)^2} + \frac{(\gamma_d-\gamma_a)^2}{(h_a+h_d)^2}\right)$$
$$+ \frac{2[(\chi_c-\chi_a)(\gamma_d-\gamma_b)-(\gamma_c-\gamma_a)(\chi_d-\chi_b)]}{(h_a+h_b+h_c+h_d)^2\Delta^2}. \tag{3.13}$$

The calculation of (3.10–3.13) is the most demanding part of our derivation. To make the connection with (3.6), we must rewrite (3.9) as a sum over grid points. We find that

$$dH = \sum_{ij} w_{ij}[-\chi_{ij}d\zeta_{ij} - \gamma_{ij}d\mu_{ij} + \Phi_{ij}dh_{ij}] \tag{3.14}$$

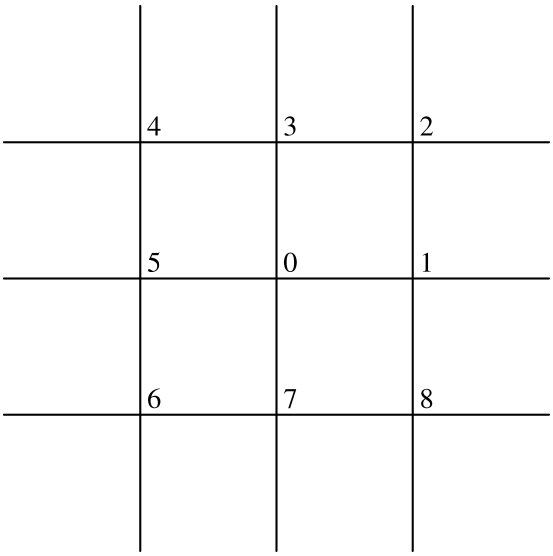

Figure 2. A representative interior grid point (numbered zero) and the 8 surrounding grid points.

where ζ_{ij}, μ_{ij} and Φ_{ij} are given by (A.4-6), after use of (3.10–3.13). Eq. (3.14) is analogous to (2.24), and (A.4-6) are the analogs of (2.8) and (2.11). We prove conservation of the finite-difference energy (3.7-3.8) in a manner analogous to Section 2: Dividing (3.14) by dt, and making use of (3.6), we find that $dH/dt = 0$.

Eqs. (A.1-3) include external forcing terms, which will be discussed in Section 5. If these forcing terms are omitted, then the coupled ordinary differential equations (A.1-6) exactly conserve the energy (3.7-3.8) and the Casimirs (3.5). Eqs. (A.1) and (A.4), which apply at interior gridpoints, are identical to (3.15) and (3.19) in S07. The subscripts in (A.1) and (A.4) refer to the representative interior grid point in Figure 2. We use (A.1-3) to step the variables ζ, μ, h forward in time at all grid points, including boundary points. Then, at the new time, we use (A.4-6) to determine χ, γ, Φ at all the interior points, and γ, Φ at all the boundary points. Once again, $\chi = 0$ at boundary gridpoints; (A.2-3) and (A.5-6) incorporate this boundary condition. Since χ vanishes at boundary points, the boundary points make no contribution to $-\chi_{ij} d\zeta_{ij}$ in (3.14); for this reason there is no analog of (A.4a) in (A.5) or (A.6). Thus (A.4-6) comprise the same number of equations as the number of unknown values of χ, γ, Φ. The streamfunction χ is uniquely determined, but remains γ undetermined by a (physically irrelevant) constant.

Figure 2

Nowhere in the preceding derivation was it necessary to prescribe a finite-difference form of the boundary conditions (2.9b) or (2.10); our insistence upon conservation laws has been sufficient by itself to produce a closed, finite-difference dynamics. However, if this finite-difference dynamics is a good approximation to shallow water dynamics, then the boundary conditions must somehow be contained within it. The next section shows

how this occurs, and how the method can be generalized to the case of multiply connected boundaries.

4. One-dimensional example

In this section we consider rotating, y-independent flow in an infinite channel with boundaries at $x = 0$ and $x = L$. The derivation of our model equations is transparent in this one-dimensional case, and we see, more clearly than in the preceding more general derivation, how the model incorporates the boundary conditions. To test our model, we compare its solutions to those of a one-dimensional Lagrangian model with high expected accuracy.

The one-dimensional equations analogs of (2.6), (2.8) and (2.11) are

$$\zeta_t = -(q\gamma_x)_x \tag{4.1a}$$

$$\mu_t = (q\chi_x - \Phi_x)_x \tag{4.1b}$$

$$h_t = -\gamma_{xx} \tag{4.1c}$$

$$(h^{-1}\chi_x)_x = \zeta \tag{4.2a}$$

$$(h^{-1}\gamma_x)_x = \mu \tag{4.2b}$$

$$\Phi = gh + \frac{1}{2h^2}\left(\chi_x^2 + \gamma_x^2\right) \tag{4.2c}$$

where subscripts denote differentiation, and $q = (f+\zeta)/h$ with f a constant. As boundary conditions we take

$$\gamma_x = 0 \tag{4.3a}$$

$$q\chi_x - \Phi_x = 0 \tag{4.3b}$$

at $x = 0, L$. In this case we may take $\chi = 0$ at one of the boundaries, but the value of χ at the other boundary remains to be determined, because, when $f \neq 0$, the cross-channel integral of $vh = \chi_x$ varies with time. Using only (4.1) and (4.3) we obtain the one-dimensional analog

$$\int dx(A\zeta_t + B\mu_t + Ch_t) = \int dx(qA_x\gamma_x - q\chi_x B_x + \Phi_x B_x + C_x\gamma_x) \tag{4.4}$$

of (2.14). We discretize this as

$$\begin{aligned}\sum_{i=1}^{n} w_i(A_i\dot{\zeta}_i + B_i\dot{\mu}_i + C_i\dot{h}_i)&\\ = \frac{1}{\Delta^2}\sum_{i=1}^{n-1}\Bigg[\frac{1}{2}(q_i + q_{i+1})[(A_{i+1} - A_i)(\gamma_{i+1} - \gamma_i) - (B_{i+1} - B_i)(\chi_{i+1} - \chi_i)]&\\ + [(B_{i+1} - B_i)(\Phi_{i+1} - \Phi_i) + (C_{i+1} - C_i)(\gamma_{i+1} - \gamma_i)]\Bigg].&\end{aligned} \tag{4.5}$$

Here, $i = 1$ and $i = n$ correspond to the boundaries, and we take $w_i = 1$ except $w_1 = w_n = 1/2$. The over-dots denote d/dt. Differentiating (4.5) with respect to each A_i, B_i, C_i yields the prognostic equations analogous to (4.1),

$$\dot{\zeta}_1 = \frac{1}{\Delta^2}(q_1 + q_2)(\gamma_1 - \gamma_2) \tag{4.6a}$$

$$\dot{\zeta}_i = \frac{1}{2\Delta^2}[(q_{i-1} + q_i)(\gamma_i - \gamma_{i-1}) + (q_{i+1} + q_i)(\gamma_i - \gamma_{i+1})], \quad i = 2, \ldots, n-1 \tag{4.6b}$$

$$\dot{\zeta}_n = \frac{1}{\Delta^2}(q_{n-1} + q_n)(\gamma_n - \gamma_{n-1}) \tag{4.6c}$$

$$\dot{\mu}_1 = \frac{1}{\Delta^2}(q_1 + q_2)(\chi_2 - \chi_1) + \frac{2}{\Delta^2}(\Phi_1 - \Phi_2) \tag{4.7a}$$

$$\dot{\mu}_i = \frac{1}{2\Delta^2}[(q_{i-1} + q_i)(\chi_{i-1} - \chi_i) + (q_{i+1} + q_i)(\chi_{i+1} - \chi_i)] + \frac{1}{\Delta^2}(2\Phi_i - \Phi_{i-1} - \Phi_{i+1}), \quad i = 2, \ldots, n-1 \tag{4.7b}$$

$$\dot{\mu}_n = \frac{1}{\Delta^2}(q_{n-1} + q_n)(\chi_{n-1} - \chi_n) + \frac{2}{\Delta^2}(\Phi_n - \Phi_{n-1}) \tag{4.7c}$$

$$\dot{h}_1 = \frac{2}{\Delta^2}(\gamma_1 - \gamma_2) \tag{4.8a}$$

$$\dot{h}_i = \frac{1}{\Delta^2}(2\gamma_i - \gamma_{i-1} - \gamma_{i+1}), \quad i = 2, \ldots, n-1 \tag{4.8b}$$

$$\dot{h}_n = \frac{2}{\Delta^2}(\gamma_n - \gamma_{n-1}). \tag{4.8c}$$

Eqs. (4.6-4.8), which step the ζ_i, μ_i, h_i forward in time at all grid points, including boundary grid points, automatically conserve mass, circulation, and potential enstrophy in the forms

$$\sum_{i=1}^{n} w_i h_i, \quad \sum_{i=1}^{n} w_i h_i q_i, \quad \sum_{i=1}^{n} w_i h_i q_i^2 \tag{4.9}$$

for arbitrary values of the χ_i, γ_i, Φ_i.

To close the dynamics, we must determine the diagnostic variables χ_i, γ_i, Φ_i in terms of the ζ_i, μ_i, h_i. As in Section 3, we begin by writing down a discrete form of the energy,

$$H = K + \sum_{i=1}^{n} \frac{1}{2} w_i g h_i^2 \tag{4.10}$$

where

$$K = \sum_{i=1}^{n-1} \left\{ \frac{1}{\Delta^2} \frac{[(\chi_{i+1} - \chi_i)^2 + (\gamma_{i+1} - \gamma_i)^2]}{(h_i + h_{i+1})} \right\}. \tag{4.11}$$

Then

$$dH = dK + \sum_{i=1}^{n} w_i g h_i dh_i \tag{4.12}$$

where

$$dK = \sum_{i=1}^{n-1} \frac{1}{\Delta^2} \left\{ 2(\chi_{i+1} - \chi_i) d\left[\frac{(\chi_{i+1} - \chi_i)}{(h_i + h_{i+1})}\right] + \frac{(\chi_{i+1} - \chi_i)^2}{(h_i + h_{i+1})^2} d(h_i + h_{i+1}) \right.$$
$$\left. + 2(\gamma_{i+1} - \gamma_i) d\left[\frac{(\gamma_{i+1} - \gamma_i)}{(h_i + h_{i+1})}\right] + \frac{(\gamma_{i+1} - \gamma_i)^2}{(h_i + h_{i+1})^2} d(h_i + h_{i+1}) \right\}. \tag{4.13}$$

Substituting (4.13) into (4.12) we have

$$dH = \sum_{i=1}^{n} w_i (-\chi_i d\zeta_i - \gamma_i d\mu_i + \Phi_i dh_i) \tag{4.14}$$

where

$$\zeta_1 = \frac{4}{\Delta^2} \frac{(\chi_2 - \chi_1)}{(h_1 + h_2)} \tag{4.15a}$$

$$\zeta_i = \frac{2}{\Delta^2} \left[\frac{(\chi_{i-1} - \chi_i)}{(h_{i-1} + h_i)} + \frac{(\chi_{i+1} - \chi_i)}{(h_{i+1} + h_i)} \right], \quad i = 2, \ldots, n-1 \tag{4.15b}$$

$$\zeta_n = \frac{4}{\Delta^2} \frac{(\chi_{n-1} - \chi_n)}{(h_{n-1} + h_n)} \tag{4.15c}$$

$$\mu_1 = \frac{4}{\Delta^2} \frac{(\gamma_2 - \gamma_1)}{(h_1 + h_2)} \tag{4.16a}$$

$$\mu_i = \frac{2}{\Delta^2} \left[\frac{(\gamma_{i-1} - \gamma_i)}{(h_{i-1} + h_i)} + \frac{(\gamma_{i+1} - \gamma_i)}{(h_{i+1} + h_i)} \right], \quad i = 2, \ldots, n-1 \tag{4.16b}$$

$$\mu_n = \frac{4}{\Delta^2} \frac{(\gamma_{n-1} - \gamma_n)}{(h_{n-1} + h_n)} \tag{4.16c}$$

$$\Phi_1 = g h_1 + \frac{2}{\Delta^2} \left[\frac{(\chi_2 - \chi_1)^2}{(h_1 + h_2)^2} + \frac{(\gamma_2 - \gamma_1)^2}{(h_1 + h_2)^2} \right] \tag{4.17a}$$

$$\Phi_i = g h_i + \frac{1}{\Delta^2} \left[\frac{(\chi_{i-1} - \chi_i)^2}{(h_{i-1} + h_i)^2} + \frac{(\chi_{i+1} - \chi_i)^2}{(h_{i+1} + h_i)^2} \right.$$
$$\left. + \frac{(\gamma_{i-1} - \gamma_i)^2}{(h_{i-1} + h_i)^2} + \frac{(\gamma_{i+1} - \gamma_i)^2}{(h_{i+1} + h_i)^2} \right], \quad i = 2 \ldots n-1 \tag{4.17b}$$

$$\Phi_n = g h_n + \frac{2}{\Delta^2} \left[\frac{(\chi_{n-1} - \chi_n)^2}{(h_{n-1} + h_n)^2} + \frac{(\gamma_{n-1} - \gamma_n)^2}{(h_{n-1} + h_n)^2} \right]. \tag{4.17c}$$

The motivation for (4.14) is the same as for (2.24) and (3.14). Eqs. (4.15-17) are the analogs of (4.2a-c). Eqs. (4.15) and (4.16) have no solutions for χ and γ unless the vorticity and divergence obey the consistency relations

$$\sum_{i=1}^{n} w_i \zeta_i = 0 \tag{4.18}$$

$$\sum_{i=1}^{n} w_i \mu_i = 0. \tag{4.19}$$

Eq. (4.19) is the finite-difference analog of $\int dx\, \mu = \int dx\, u_x = 0$, which follows from the boundary condition of no normal flow. However, the lhs of (4.18) is the finite-difference analog of

$$\int dx\, \zeta = \int dx\, v_x = v(x = L) - v(x = 0) \tag{4.20}$$

which does not generally vanish. In fact, the values of v at the channel boundaries are conserved constants of the motion. This points to a needed modification of (4.15a) and (4.15c) that does not affect the other conservation laws.

To see what modification is required, we perform a Taylor expansion of (4.15a) about the point $x = 0$ with the result

$$\zeta = \frac{2}{\Delta} v + (h^{-1}\chi_x)_x + O(\Delta). \tag{4.21}$$

This shows that the term $-2v_1/\Delta$ must be added to the rhs of (4.15a), where v_1 is the constant value of the along-channel velocity at the boundary. Then, instead of (4.21), we have

$$\zeta = \frac{2}{\Delta}(v - v_1) + (h^{-1}\chi_x)_x + O(\Delta). \tag{4.22}$$

To leading order (4.22) corresponds to the boundary condition $v = v_1$, and to next order it produces (4.2a). Similar remarks apply to the other boundary, and thus (4.15) must be replaced by

$$\zeta_1 = \frac{4}{\Delta^2}\frac{(\chi_2 - \chi_1)}{(h_1 + h_2)} - \frac{2}{\Delta} v_1 \tag{4.23a}$$

$$\zeta_i = \frac{2}{\Delta^2}\left[\frac{(\chi_{i-1} - \chi_i)}{(h_{i-1} + h_i)} + \frac{(\chi_{i+1} - \chi_i)}{(h_{i+1} + h_i)}\right], \quad i = 2, \ldots, n-1 \tag{4.23b}$$

$$\zeta_n = \frac{4}{\Delta^2}\frac{(\chi_{n-1} - \chi_n)}{(h_{n-1} + h_n)} + \frac{2}{\Delta} v_n. \tag{4.23c}$$

Our final, complete, finite difference equations are (4.6–4.8), (4.16–4.17) and (4.23). These equations *exactly* conserve the Casimirs (4.9) and the energy (4.10–4.11), because v_1 and v_n

and are treated as constants. A complete set of initial data consists of the values of ζ_i, μ_i, h_i at *all* grid points, and either v_1 or v_n. The latter two conserved constants are related by

$$\sum_{i=1}^{n} w_i \zeta_i \Delta = v_n - v_1 \tag{4.24}$$

which is the analog of (4.20). By (4.6), the time derivative of the lhs of (4.24) vanishes, so this consistency condition is maintained. Similar remarks apply to the divergence with its consistency condition (4.19). To solve (4.16) and (4.23) we set $\chi_1 = \gamma_1 = 0$ and solve for the $n-1$ remaining χ_i's and γ_i's by successive use of (4.16b) and (4.23b); there is no need for a tridiagonal solver. The consistency conditions guarantee satisfaction of (4.16c) and (4.23c).

In summary, by solely emphasizing conservation laws, we have produced a finite-difference dynamics that faithfully represents (4.1–4.3). This finite-difference formulation blends the analytical equations and the the analytical boundary conditions in a curious way: Just as (4.23a) blends (4.2a) with the boundary condition $v = v_1$; (4.16a) blends (4.2b) and the boundary condition (4.3a); (4.6a) blends (4.1a) and (4.3a); and (4.7a) blends (4.1b) and (4.3b). This formulation is *not* likely to have resulted from direct approximations to (4.1–4.3) by any standard method, but it seems to be the inevitable result of maintaining the conservation laws.

Do the conservation laws guarantee a superior model? That question can really only be answered by comparison to nontrivial exact solutions. Unfortunately, even in one space dimension, nontrivial analytical solutions to the rotating shallow water equations seem non-existent when boundaries are present. However, we argue that numerical solutions of a Lagrangian formulation of this problem deserve to be considered quasi-analytical, and in the remainder of this section we compare solutions of the model derived above to solutions of the Lagrangian model.

In the Lagrangian formulation (see, for example, Zeitlin, 2007), the fundamental dependent variable is $x(a, t)$ where a is a fluid particle label assigned so that

$$h(a, t) = H/x_a. \tag{4.25}$$

Here H is the mean depth and $a = 0(L)$ at $x = 0(L)$. A time-integral of the y-direction momentum equation (4.34b) yields

$$v(a, t) = -f\, x(a, t) + K(a) \tag{4.26}$$

where $K(a)$ is defined by

$$K(a) = v_0 + H \int_0^a q(a')\, da', \tag{4.27}$$

v_0 is the prescribed (constant) value of v at the left boundary $x = 0$, and $q(a)$ is the prescribed potential vorticity on fluid particles. The only prognostic equation is the x-direction momentum equation,

$$x_{tt} + f^2 x = f K(a) + c^2 x_{aa}/(x_a)^3 \tag{4.28}$$

where $c^2 = gH$. To solve the Lagrangian model, we prescribe v_0 and $q(a)$ [and hence $K(a)$], and we solve (4.28) subject to the initial conditions $x(a, 0)$ and $x_t(a, 0)$. Eqs. (4.25–4.27) incorporate the conservation laws for mass and for potential vorticity *on fluid particles*. Thus (4.28) *automatically* conserves all of the Casimir invariants.

Bühler (1993) gives exact, analytical, progressive-wave solutions of (4.28), but these exact solutions do not generalize to the case of boundaries. However, it is easy to construct a discrete, energy-conserving analog of (4.28), because (4.28) is equivalent to Hamilton's principle in the form

$$0 = \delta \int dt\ L = \delta \int dt \int da\ [(x_t)^2 - f^2 x^2 - c^2/x_a + 2 f K(a)\ x] \tag{4.29}$$

for particle-location variations $\delta x(a, t)$ that vanish at the rigid boundaries. The finite-difference approximation

$$L = \frac{1}{2} \sum_{i=1}^{n-1} \left[\left(\dot{x}_i^2 + \dot{x}_{i+1}^2\right) - f^2 \left(x_i^2 + x_{i+1}^2\right) - \frac{2c^2 \Delta}{(x_{i+1} - x_i)} + 2 f (K_i x_i + K_{i+1} x_{i+1}) \right] \tag{4.30}$$

yields the analog

$$\ddot{x}_i + f^2 x_i = \frac{c^2 \Delta}{2} \left[\frac{1}{(x_i - x_{i-1})^2} - \frac{1}{(x_i - x_{i+1})^2} \right] + f K_i, \quad i = 2, \ldots, n-1 \tag{4.31}$$

of (4.28), with $x_1 = 0$ and $x_n = L$. Here Δ is the grid spacing in a-space. If both the Eulerian and Lagrangian models have the same number of grid points, then Δ has the same value (in units of length) in both models. Solution of (4.31) yields $u_i = \dot{x}_i$,

$$h_{i+1/2} = \frac{H \Delta}{(x_{i+1} - x_i)} \tag{4.32}$$

and

$$v_i = -f\ x_i + K_i \tag{4.33}$$

which may be directly compared to the solutions of the previously derived Eulerian model. This comparison is severe because, once again, the Lagrangian model (4.31–4.33) exactly

conserves the mass and the potential vorticity *on particles*, and exactly incorporates the boundary conditions on both components of velocity. In fact, the only serious approximation in the Lagrangian model is the finite-difference on the rhs of (4.31). If one were solely interested in one-dimensional flows, then one would certainly be foolish not to adopt the Lagrangian formulation.

We nondimensionalize by setting $g = H = L = 1$. Then f is the Burger number, the ratio of the domain size to the deformation radius, and it is the only remaining parameter in the equivalent form of the equations,

$$Du/Dt - fv = -h_x \tag{4.34a}$$

$$Dv/Dt + fu = 0 \tag{4.34b}$$

$$h_t + (hu)_x = 0. \tag{4.34c}$$

We consider cases in which the initial x-direction velocity vanishes, $u = x_t(a, 0) = 0 = \mu(x, 0)$. The remaining initial data are $h(x, 0)$ and $v(x, 0)$, which determine $\zeta(x, 0)$, $x(a, 0)$, v_0 and $q(a)$. If f is too small, then shocks may appear after a short time. These shocks could be avoided by adding viscosity to the models, and in Section 5 we explain how to do this. Here we compare purely inviscid solutions. Therefore all of our solutions terminate before shocks occur, that is, before $x_{i+1} \le x_i$ for any i.

A large number of cases have been examined; all show excellent agreement between the two models. We show only two cases. Both have $f = 5$ (5 deformation radii across the domain) and 200 grid points. Figure 3 shows u, v, and h at 6 times between $t = 0$ and $t = 2$ in a case especially chosen to test the unconventional implementation of the boundary conditions in the Eulerian model. The initially unbalanced state $h(x, 0) = 1$, $u(x, 0) = 0$, and $v(x, 0) = 0.1$ produces a positive initial Du/Dt that is the same at all grid points *except* the boundary points, where Du/Dt must vanish. This drastic change in initial behavior—from maximum to vanishing Du/Dt over a distance of one grid spacing—severely tests the way in which both models handle the solid boundaries. However, at all the later times shown in Figure 3, the difference between the Eulerian model (dashed curves) and the Lagrangian model (solid curves) is almost imperceptible.

Figure 3

Figure 4 shows the solutions resulting from the initial conditions $h(x, 0) = 1$, $u(x, 0) = 0$, and $v(x, 0)$ proportional to $(x-1/2)\exp(-(x-1/2)^2/(0.02)^2)$ with a maximum value of 0.1, corresponding to very thin (4 grid points wide) regions of oppositely directed flow near the center of the channel. Such barely resolved cases are important because, in turbulent solutions of the two-dimensional case, the smallest scales of motion are always minimally resolved. Because the unbalanced initial condition is highly localized, the solutions of Figure 4 exhibit a high degree of geostrophic adjustment: Although inertia-gravity waves cannot escape the bounded domain, the mid-channel flow attains approximate geostrophic balance. Again, despite the relatively poor resolution, the agreement between the two models is excellent despite the huge differences in their construction.

Figure 4

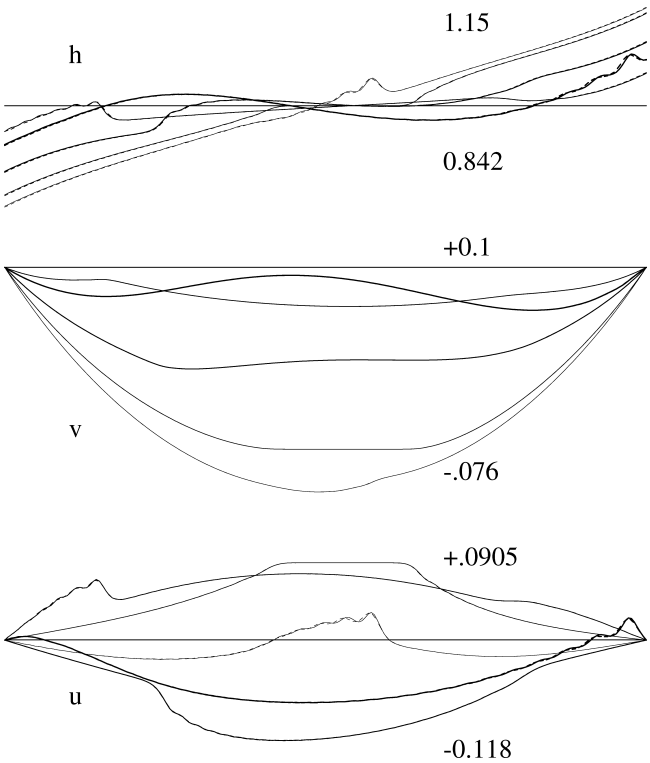

Figure 3. The velocity (u, v) and depth h in a one-dimensional solution of the rotating shallow-water equations with Coriolis parameter $f = 5.0$ at the six times $t = 0, 0.4, 0.8, 1.2, 1.4, 2.0$. Darker contours correspond to later times. The initial conditions correspond to a flat surface, $h = 1.0$, and a uniform velocity $v = 0.1$ into the page. The u-velocity vanishes initially, and at the boundaries $x = 0, 1$. Solid curves represent solutions of the Lagrangian model (4.31-33). Dashed curves represent solutions of the Eulerian model (4.6-8), (4.16-17) and (4.23). Despite the large differences in their formulations, the two models agree so closely that the dashed and solid curves are indistinguishable. Numerical values are the extremes of each plot.

5. Two-dimensional solutions

S07 presented two-dimensional solutions of (A.1) and (A.4) for the case of infinitely periodic flow with constant f. These solutions agreed closely with the corresponding solutions of the AL model, which also conserves energy and potential enstrophy. However, the solutions of two other models—one conserving energy but not potential enstrophy, the other conserving potential enstrophy but not energy—were less accurate in the sense that they agreed with the fully conservative solutions only at a higher resolution and for a limited time.

The solutions described in S07 exhibited strong vortex interactions in the absence of boundaries. In this section we present two-dimensional solutions of (A.1-6) in a bounded domain, and we focus on solutions that interact strongly with the boundaries. The

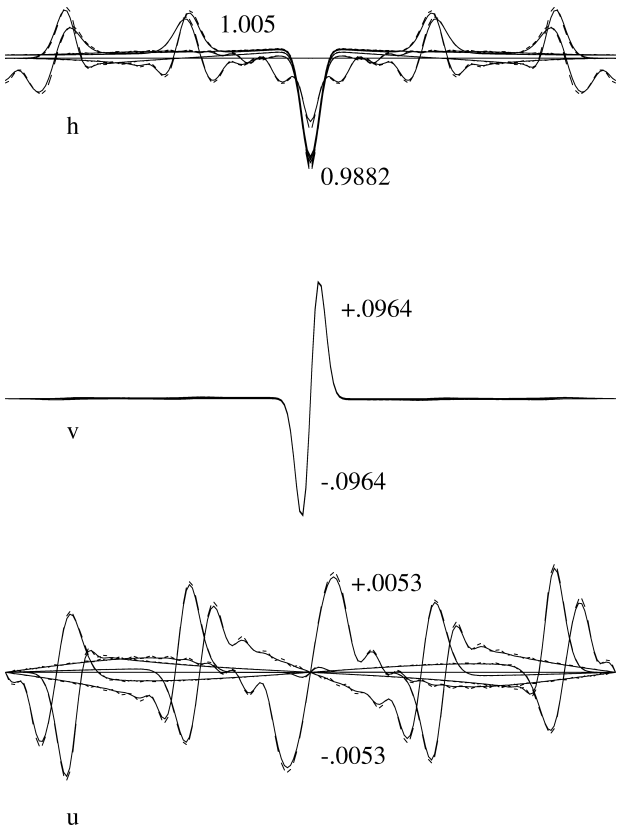

Figure 4. The same as Figure 3, but for an initial condition in which the velocity into the page has the form shown in the middle plot. (This component of velocity experiences negligible change.) As in figure 3, the solid and dashed curves are nearly indistinguishable.

boundaries are the new feature of the present paper in relation to S07. To give the solutions an oceanographic flavor, we regard our shallow-water model as a reduced gravity model of the ocean's upper layer. Hence we take $g = 0.002 \times 9.8\,\mathrm{m\,sec^{-2}}$ and mean depth $H = 500\,\mathrm{m}$. Then $c = \sqrt{gH} = 270\,\mathrm{km\,day^{-1}}$. We consider a square ocean of side $L = 4000\,\mathrm{km}$, and we take $\Delta = 30.2\,\mathrm{km}$, corresponding to the very modest resolution of 129^2 grid points.

Because this paper primarily addresses the ideal, inviscid part of shallow water dynamics, we examine inviscid solutions. Of course, sub-grid scale viscosity is always eventually required to prevent potential enstrophy from accumulating at the smallest resolved scales, and below we add viscosity to our model. However, it is worthwhile to run the model for limited times in perfect-fluid mode, that is, without viscosity, and with no-normal-flow as the only the boundary condition.

The inviscid equations (A.1-6) comprise a closed set of ordinary differential equations in the gridded values of the six variables ζ, μ, h, χ, γ, Φ. These coupled ordinary differential

equations conserve the mass, circulation, and potential enstrophy in the forms (3.5), and the energy in the form (3.7-8). Considered as approximations to the shallow water equations, both the dynamical equations (A.1-A.6) and the conserved quantities (3.5,3.7-8) contain spatial truncation error. Nevertheless (A.1-6) conserve (3.5,3.7-8) *exactly*.

To solve (A.1-6) we must replace the time derivatives in (A.1-3) by a finite-difference time step, and we must solve (A.4-6) by an iteration method. In this paper we use Runge-Kutta methods to solve (A.1-3), and we use a multi-grid method to solve (A.4-6). Both the Runge-Kutta time-step and the multi-grid solver introduce errors that affect the conservation of (3.5,3.7-8). The time-step error—resulting from truncation error in the time step—affects both the conservation of energy and the conservation of the Casimirs. The iteration error—resulting from incomplete convergence of the multi-grid solver—affects only the conservation of the energy, because (A.1-3) conserve the Casimirs (3.5) for any values of χ, γ, Φ. Departures from exact conservation can be used to gauge these two sources of error. As we shall see, both errors are typically very small, and can be made as tiny as desired.

First we consider inviscid, non-rotating ($f = 0$) flow with initial conditions $h = H$ (constant), $\mu = 0$, and

$$\zeta(x, y, 0) = A \exp[-(x^2 + (y - {y_0}^2)/d^2] + A \exp[-(x^2 + (y + {y_0}^2))/d^2] \qquad (5.1)$$

where $y_0 = 250\,\text{km}$ and $d = 500\,\text{km}$, corresponding to counter-rotating vortices that propel each other toward the eastern boundary. The amplitude A corresponds to a maximum velocity of $103.7\,km\,\text{day}^{-1}$, i.e. to a Froude number of about 0.4. Figure 5 shows the divergence μ (left) and vorticity ζ (right) after 30, 60 and 90 days. The final maximum velocity is $91.6\,\text{km day}^{-1}$. During this period of about 15,500 time steps, the energy—computed as kinetic plus *available* potential energy—is always within 0.039% of its initial value, and the potential enstrophy is always within an even smaller factor of 10^{-7} of its initial value.

Figure 5

For the experiment depicted in Figure 5, we used second-order Runge-Kutta (also called the 'midpoint method', e.g. Durran, 1999, p. 53) with time-step $\Delta t = 0.05\Delta/c$. To assess the sensitivity of our results to the method of time-stepping, we repeated this experiment with fourth-order Runge-Kutta (ibid, pp. 65-71), and with an *adaptive* fourth-order Runge-Kutta scheme. For the latter, we followed the method of Dukowicz and Greatbatch (1999, pp. 1850-1851), in which the time step is continually adjusted to keep the maximum difference between the new values of ζ and μ, as computed by second-order and fourth-order Runge-Kutta, to within the prescribed fractional amount $\epsilon = 10^{-4}$. This value of ϵ corresponded to an average time step of $\langle \Delta t \rangle = 0.0533 \Delta x/c$. The results of these and other experiments showed that the fourth-order time steps resulted in negligible improvement to the already high accuracy of the calculation, as measured by the maximum departure of the energy and potential enstrophy from their initial values.

In every case, the potential enstrophy was conserved to a higher accuracy than the energy, suggesting that overall accuracy could be improved by increasing the number of iterations

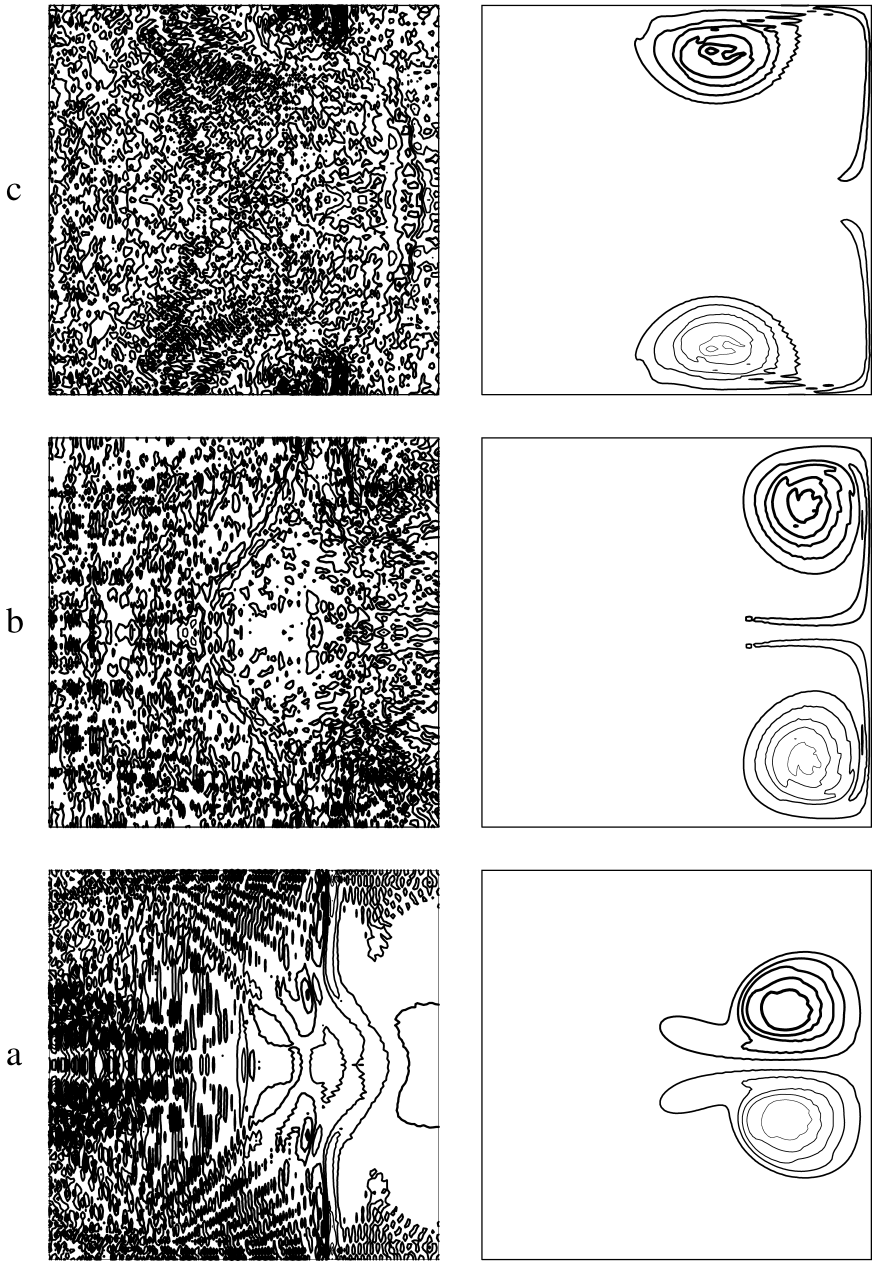

Figure 5. The divergence μ (left) and vorticity ζ (right) in an *inviscid*, square, nonrotating ocean at (a) 30 days, (b) 60 days, and (c) 90 days after the initial conditions (5.1) corresponding to counter-rotating vortices at mid-basin. Darker contours correspond to larger values.

in the multi-grid solver, which affects only the conservation of energy. We solve (A.4-6) for χ and γ by an adaption of the multigrid method of Press et al (1992, pp. 862-880). The accuracy of the multi-grid solutions can easily be checked by *a posteriori* evaluation of the two sides of (A.4a) and (A.4b). With the iteration parameters set at 'npre'=2, 'npost'=1, 'ncycle'=2 (ibid, p. 869), we find agreement to 4 significant figures. When these three iteration parameters are doubled, we find agreement to 5 significant figures, and we find that the error in the energy conservation is decreased from the value 0.039% reported above to 0.00015%. However, the higher iteration settings increase the computation time by a factor 2.8. In all the experiments performed, the fields of ζ, μ and h showed no significant sensitivity to the method of time step or to the iteration settings, except at the very small scales comparable to the grid-spacing. At these very small scales, the flow is 'chaotic', i.e. inherently sensitive to a small change in *anything*.

All of the numerical experiments actually depicted in this paper use second-order Runge-Kutta with $\Delta t = 0.05\Delta/c$, and with the former, lower, 2-1-2 settings of the iteration parameters. All the depicted experiments conserve the energy to within a tiny fraction of one per cent, and conserve potential enstrophy to within an even smaller fraction. If greater accuracy is required, then the multi-grid solver can be forced to converge, to machine accuracy if desired, by increasing the values of the iteration parameters. However, this seems pointless considering the already high accuracy of the 2-1-2 iteration settings, the spatial truncation error *implicit* in (A.1-6), and the fact that even in the case of the 2-1-2 settings, the multi-grid solver consumes 95% of the computation time. The solution of the elliptic equations (A.4a) and (A.4b) is thus the most time-consuming part of our calculation, and it is the primary disadvantage of our method. We come back to this point in Section 6.

Next we incorporate viscosity into our model. To maintain the ability to run the model in either viscous or perfect-fluid mode, we incorporate viscosity by a Strang-splitting of the dynamics (e.g. Durran, 1999. pp. 131-132), in which the perfect-fluid equations are advanced one time step, followed by a one-time-step advance of the viscous dynamics. Strang splitting requires that the time step for each split be 'self contained:' it must advance the system from one time to the next without referring to earlier or later times. Runge Kutta schemes are ideal for this purpose. For the viscous dynamics we take

$$\frac{\partial \zeta}{\partial t} = \nu \nabla^2 \zeta \tag{5.2a}$$

$$\frac{\partial \mu}{\partial t} = \nu \nabla^2 \mu \tag{5.2b}$$

with boundary conditions

$$\zeta = 0 \tag{5.3a}$$

$$\nabla \mu \cdot \mathbf{n} = 0. \tag{5.3b}$$

The precise form (5.2-5.3) is a matter of convenience: Since it does not involve χ and γ, we do not require additional solutions of the diagnostic equations (A.4-6). We use the simplest (5-point) discrete forms of (5.2) and the consistent discretization of (5.3b). In each viscous step, we enforce (5.3a) at boundary points, and we apply (5.2a) only at interior points. The boundary condition (5.3a) is sometimes called free slip. The boundary condition (5.3b) maintains the important consistency condition (5.7).

Figure 6 shows the divergence μ (left) and vorticity ζ (right) in a solution with the same initial conditions (5.1) as that shown in Figure 5, but with viscosity $\nu = 0.00623 u_{max}\Delta$, where u_{max} is the initial maximum velocity. After 90 days, this small viscosity consumes only 2.75% of the energy—the final maximum velocity is 86.2 km day^{-1}—but it is sufficient to wipe out most of the poorly resolved features in the divergence field. However, the shapes and locations of the main flow features are the same as in the inviscid solution of Figure 5. **Figure 6**

Figure 7 represents a low-pass filter of the inviscid results shown in Figure 5. More precisely, Figure 7 shows the same fields shown in Figure 5, but after two passes of an Asselin filter (Durran, 1999 p. 62) invoked to remove the grid-scale oscillations in μ and ζ. This purely cosmetic, *a posteriori* smoothing of the inviscid dynamics should be compared to the fields in Figure 6, on which viscosity operated throughout the calculation. The similarity between Figures 6 and 7 shows that viscosity plays no very essential role in this case, and is certainly not required to stabilize our model. **Figure 7**

Next we consider inviscid flow on the equatorial beta plane. We take $f = \beta y$ with $\beta = 4\pi$ day^{-1}/(6400 km) and the equator, $y = 0$, at mid-basin. The equatorial deformation radius $r_{eq} = \sqrt{c/2\beta} = 262$ km, and the Rossby radius, c/f, at the northern boundary is 69 km. The initial conditions

$$h(x, y, 0) = H + \eta_0 \exp\left(-r^2/4r_{eq}^2\right) \tag{5.4a}$$

$$\zeta(x, y, 0) = \frac{c\eta_0}{2Hr_{eq}^2} y \exp\left(-r^2/4r_{eq}^2\right) \tag{5.4b}$$

$$\mu(x, y, 0) = -\frac{c\eta_0}{2Hr_{eq}^2} x \exp\left(-r^2/4r_{eq}^2\right) \tag{5.4c}$$

where $\eta_0 = 0.1H$ and $r^2 \equiv x^2 + y^2 = 0$ at mid-basin, correspond to a circular thermocline depression at the center of the ocean. On the *infinite* equatorial beta-plane, the state (5.4) would propagate eastward, as an equatorial Kelvin wave, at speed c with no change in its form; see Gill (1982, Eq. 11.5.5). Figure 8 (a) shows the divergence μ (left) and vorticity ζ (right) at the time required for the thermocline depression to reach the eastern boundary. According to theory, most of this energy propagates poleward in coastal Kelvin waves, which are estimated to reach the midpoints of the poleward boundaries at the time shown in Figure 8 (b). Figure 8 (c) corresponds to the time estimated for the main disturbance to **Figure 8**

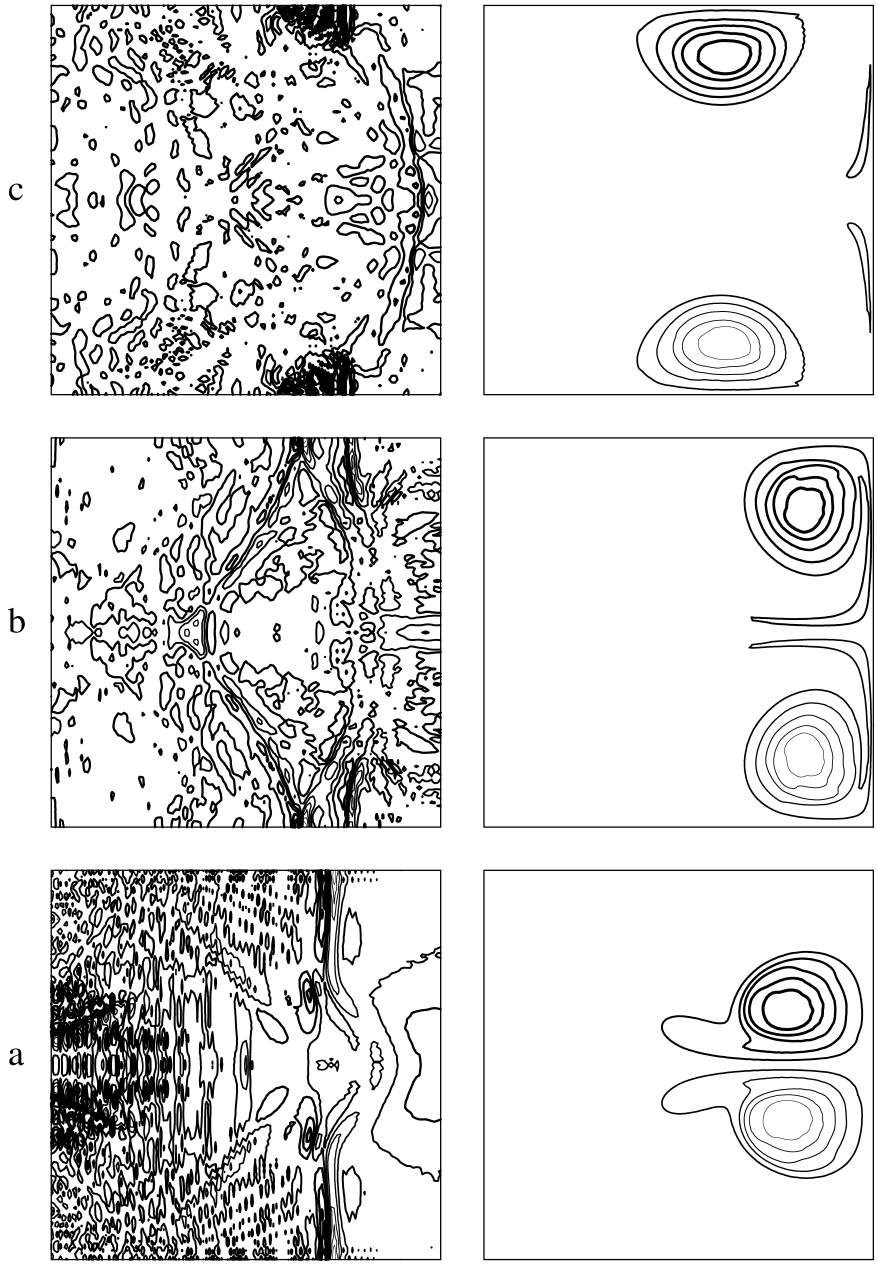

Figure 6. The same as Figure 5, but with a small nonzero viscosity. The viscosity smoothes the smallest scales of motion, but wipes out only 2% of the energy.

Figure 7. *A posteriori* smoothing of the inviscid fields shown in Figure 5 resembles the viscous results of Figure 6.

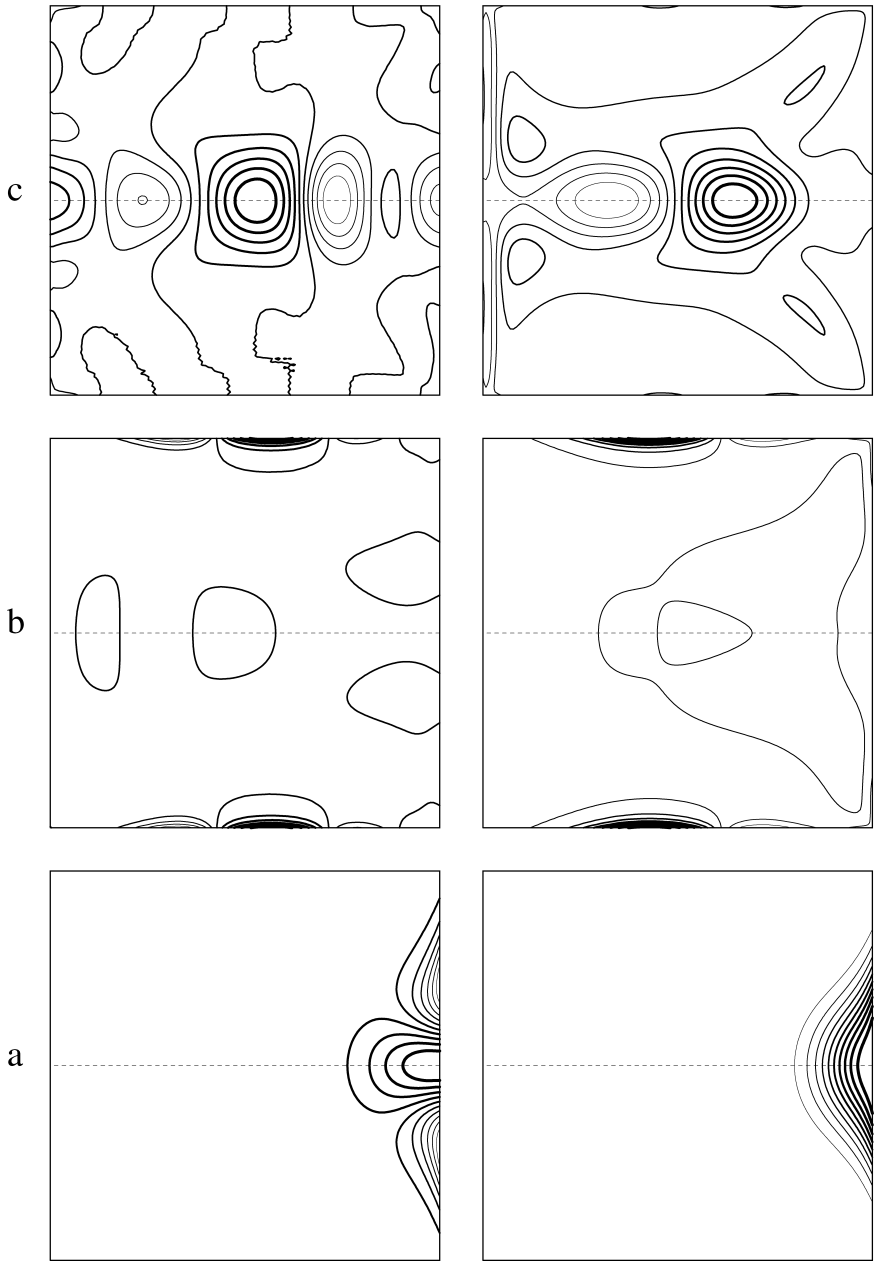

Figure 8. The divergence μ (left) and vorticity ζ (right) in an inviscid solution with initial condition (5.4), corresponding to a thermocline depression at mid-basin. The dashed line is the equator. After 7.39 days (a), the equatorial-Kelvin pulse reaches the eastern boundary, where it splits into poleward propagating coastal Kelvin waves. These reach the midpoint of the poleward boundary at 21.7 days (b), and return, approximately, to mid-basin after 43.4 days (c). Wavenumber-dependent phase shifts at each corner-turning cause the initial pulse to be dispersed. Darker contours correspond to larger values.

return, approximately, to its initial location.[2] This experiment was chosen to test for spurious boundary reflections, especially at the corners. No such behavior is evident in Figure 8.

Finally we generalize the model of Section 3 to include an arbitrary, externally imposed body force, $D\mathbf{u}/Dt = \cdots + \mathbf{F}$, where $\mathbf{F} = (F, G)$. The normal component of $\mathbf{F}$ appears in (2.6) and in the boundary condition (2.10). Proceeding as in Section 2, we find that the rhs of (2.14) acquires the additional terms

$$\iint d\mathbf{x}[A(G_x - F_y) - B_x F - B_y G]. \tag{5.5}$$

Therefore, to the rhs of (3.1) we add the terms

$$\begin{aligned}\frac{1}{4\Delta}\sum_{\text{gridboxes}} &[[(A_a + A_b)(G_b - G_a) + (A_c + A_d)(G_c - G_d)] \\ &- [(A_a + A_d)(F_d - F_a) + (A_b + A_c)(F_c - F_b)] \\ &+ [(F_a + F_b)(B_a - B_b) + (F_c + F_d)(B_d - B_c)] \\ &+ [(G_a + G_d)(B_a - B_d) + (G_b + G_c)(B_b - B_c)]]\end{aligned} \tag{5.6}$$

where, once again, the subscripts refer to Figure 1. Proceeding as in Section 3, we obtain the forcing terms appearing in (A.1-3). These forcing terms affect the energy, vorticity and potential enstrophy, but *not* the consistency condition

$$\sum_{ij} w_{ij}\mu_{ij} = 0 \tag{5.7}$$

associated with the discrete analog of (2.8b). The condition (5.7) is analogous to (4.19). In a simply connected domain, there is no consistency condition analogous to (4.24) because the boundary condition on (2.8a) is simply $\chi = 0$. We briefly discuss island boundaries in Section 6.

Figure 9

Figure 9 shows a solution that begins from rest and is subject to the uniform, impulsive wind stress $\tau_0 = 1.41\,\text{km}^2\,\text{day}^{-2}$, corresponding to $F = G = 1.0\,\text{km}^2\,\text{day}^{-2}/h$, directed toward the northeast corner of the ocean basin. The viscosity, which has the same value as in Figure 6, corresponds to only *one third* the value $\nu = \beta\Delta^3$ needed to resolve the Munk boundary layer (e.g. Salmon, 1998, pp. 131–137) with a thickness of one grid spacing Δ. Although the forcing is uniform, the presence of the boundaries and the variation of f with latitude produce a complicated, westwardly intensified, and very energetic response, with the maximum velocity reaching $79\,\text{km day}^{-1}$ after 70 days. After 300 days (Fig. 7, upper right) the maximum velocity has decreased to $30\,\text{km day}^{-1}$, and the solution strongly resembles the predicted final state of rest, in which the depth contours are evenly-spaced lines sloping downward to the right.

2. These time estimates include the phase shift calculated by Miles (1972); at each corner, the Kelvin wave moves ahead approximately one-eighth wavelength (for wavelengths on the order of the deformation radius) as compared to motion along the shoreline at speed c. The wavenumber dependence of these phase shifts causes the initial pulse to be dispersed.

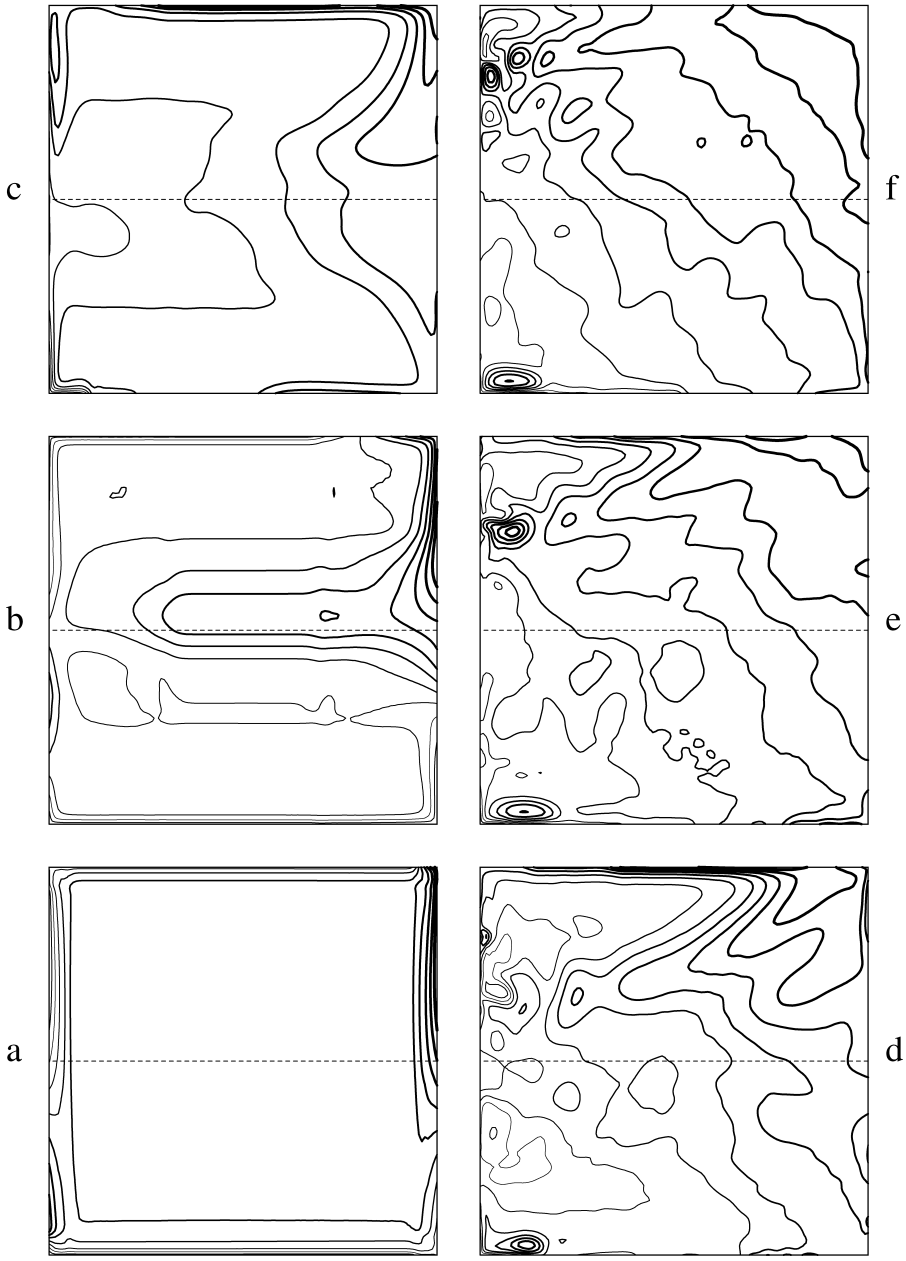

Figure 9. The thermocline depth h in a viscous solution that begins in a state of rest and is suddenly subjected to a uniform wind stress directed toward the northeast. The times shown are at 1, 5, 25, 100, 200 and 300 days. Since the wind stress has no curl, the final state is a state of rest with straight isolines of h sloping northwest to southeast. Darker contours correspond to larger values.

6. Discussion

From earliest days, two viewpoints have seemed to guide the development of numerical fluid models. Neither has, nor likely will, displace the other. In the first viewpoint, the problem is one of replacing a coupled set of partial differential equations with discrete—usually finite difference—analogs. From this first viewpoint, the conservation laws are an incidental property of the original equations, useful as a rough check on the model, but playing no significant role in its design.

In the second viewpoint, which is the viewpoint of this paper, the conservation laws are paramount, and the numerical model is designed to respect them. The model will, in hindsight, always represent a logical finite-difference approximation to the original partial differential equations, but, in this second viewpoint, this resemblance is incidental; the conservation laws are themselves the most perfect statement of the physics. Two of the earliest papers espousing the second viewpoint were those by Lorenz (1960) and Arakawa (1966); Arakawa and Lamb (1981) remains its most stunning implementation.

The present paper is one of a series of papers that have attempted to discover a general procedure, applicable to any fluid system, for deriving numerical models that retain desired conservation laws. Two of these papers (Salmon, 2005, 2007) emphasize a Nambu-bracket formulation of the physics, in which the potential enstrophy plays the role of a second Hamiltonian. The advantage of the Nambu bracket approach is that, once the Nambu bracket has been found and suitably discretized, then the conservation of energy and potential enstrophy result automatically from the antisymmetry of the bracket. The method proposed in S07 has been used by Sommer and Nevir (2009) to develop an energy- and potential-enstrophy-conserving shallow-water model on a staggered geodesic grid.

Unfortunately it seems very difficult to incorporate boundary conditions into the Nambu bracket, and hence the present paper, while retaining the general Hamiltonian approach, abandons Nambu brackets altogether. In the present paper, the derivation of the Casimir-conserving prognostic equations (A.1-3) resembles the standard finite-element procedure (e.g. Durran, 1999); it is mainly in its handling of energy conservation and boundary conditions that the paper achieves novel results. The conservation of energy determines the form of the diagnostic equations (A.4-6).

The need to solve diagnostic equations at every time step is the primary disadvantage of our model. In the calculations decribed in Section 5, the multi-grid solver accounted for 95% of the CPU time. This high cost is typical of shallow-water models that use vorticity and divergence as prognostic variables. However, despite this cost, there seems to be a trend toward formulating shallow water dynamics in these or related variables. Randall (1994) argued that spatial discretizations of the vorticity and divergence equations yield better discrete dispersion relations than the conventional formulation. Mohebalhojeh and Dritschel (2007) advocate a formulation in which the *potential* vorticity is a primary prognostic variable. Such a formulation conforms nicely to balanced models in which the potential vorticity is the *only* prognostic variable. My view is that vorticity is the essence of

fluid mechanics and will eventually form the basis of most numerical methods. Only time will tell.

A primary advantage of our model is adaptability to other geometries. For example, it would be easy to extend (A.1-6) to any domain that could be covered by square grid boxes. One need only keep track of which terms in each equation result from each surrounding grid box, and omit the appropriate terms. To accommodate islands we keep $\chi = 0$ as the boundary condition on the main coastline; then the boundary condition at each island is that χ be uniform at a value determined by the constancy of the circulation about the island. Summing the vorticity at all gridpoints—i.e., forming the two-dimensional analog of (4.24)—we find cancellation of all terms except groups of terms proportional to the value of χ at each island. The consistent, circulation-conserving boundary condition is that χ be chosen to maintain each of these groups of terms constant at its initial value. For irregularly shaped domains, it would be easy in principle to adapt our method to a domain covered by arbitrarily shaped triangles. In fact, S07 sketched the method for deriving the prognostic equations in that case. To derive the diagnostic equations, one would only need to derive the analogues of (3.10–3.13) for a representative triangle of arbitrary shape.

Although this paper represents a forward step, much remains to be done. For example, the present model does not, apparently, possess a local flux-form conservation law for momentum. It is possible to derive a model that conserves both momentum and energy, but one then loses conservation of potential enstrophy. Such tradeoffs highlight the theory's incompleteness. Although geostrophic turbulence theory assigns special significance to the potential enstrophy, potential vorticity is conserved on fluid particles, hence all the moments $\iint d\mathbf{x}\, hq^n$ are conserved. At the present time, there seems to be no method for conserving an arbitrary number of these moments in numerical models. The one-dimensional experiments in Section 4 suggest that potential enstrophy conservation captures most of the physics of potential vorticity conservation on particles (which, again, is built in to the Lagrangian model), but that may not be true in two space dimensions.

I believe that the eventual, overarching goal should be a model of the three-dimensional perfect fluid equations—either compressible or Boussinesq—with conservation of mass, momentum, energy, entropy, Ertel potential vorticity, and potential enstrophy. At the moment this seems beyond reach, but the present paper offers some clues. It suggests that the prognostic variables include the gradients of the entropy η and that the diagnostic equations respect the consistency condition $\nabla \times \nabla\eta = 0$. These diagnostic equations seem likely to be many more in number than in the exact equations, and this may be the price to be paid for maintaining so many conservation laws.

The present model grew from a need to test a theory of ocean circulation that depends upon exact conservation of energy and potential enstrophy in the inviscid limit. That application will be reported in a future publication.

Acknowledgment. This work was supported by National Science Foundation grant OCE-0542890.

APPENDIX

Summary of the two-dimensional model

This appendix collects the results of Sections 3 and 5: the discrete, inviscid shallow water equations in a rectangular domain. If an external body force $\mathbf{F} = (F, G)$ is present, then *curl* $\mathbf{F}$ appears on the rhs of (2.6a); $\nabla \cdot \mathbf{F}$ appears on the rhs of (2.6b); and $\mathbf{F} \cdot \mathbf{n}$ appears on the lhs of (2.10). Eqs. (A.1-6) represent the dynamics (2.6-2.11) with these forcing terms appended. At the representative interior point shown in Figure 2, the evolution equations analogous to (2.6) take the forms

$$\begin{aligned}
\frac{d\zeta_0}{dt} = {} & \frac{1}{12\Delta^2}[(\chi_2 + \chi_3 - \chi_7 - \chi_8)q_1 + (\chi_3 - \chi_1)q_2 \\
& + (\chi_4 + \chi_5 - \chi_1 - \chi_2)q_3 + (\chi_5 - \chi_3)q_4 \\
& + (\chi_6 + \chi_7 - \chi_3 - \chi_4)q_5 + (\chi_7 - \chi_5)q_6 \\
& + (\chi_8 + \chi_1 - \chi_5 - \chi_6)q_7 + (\chi_1 - \chi_7)q_8] \\
& + \frac{1}{2\Delta^2}[(\gamma_0 - \gamma_1)(q_0 + q_1) + (\gamma_0 - \gamma_3)(q_0 + q_3) \\
& + (\gamma_0 - \gamma_5)(q_0 + q_5) + (\gamma_0 - \gamma_7)(q_0 + q_7)] \\
& + \frac{1}{2\Delta}(G_1 - G_5) + \frac{1}{2\Delta}(F_7 - F_3) \qquad \text{(A.1a)} \\
\frac{d\mu_0}{dt} = {} & \frac{1}{2\Delta^2}[q_{0123}(\gamma_3 - \gamma_1) + q_{0345}(\gamma_5 - \gamma_3) \\
& + q_{0567}(\gamma_7 - \gamma_5) + q_{0781}(\gamma_1 - \gamma_7)] \\
& + \frac{1}{2\Delta^2}[(\chi_1 - \chi_0)(q_0 + q_1) + (\chi_3 - \chi_0)(q_0 + q_3) \\
& + (\chi_5 - \chi_0)(q_0 + q_5) + (\chi_7 - \chi_0)(q_0 + q_7)] \\
& + \frac{1}{\Delta^2}(4\Phi_0 - \Phi_1 - \Phi_3 - \Phi_5 - \Phi_7) \\
& + \frac{1}{2\Delta}(F_1 - F_5) + \frac{1}{2\Delta}(G_3 - G_7) \qquad \text{(A.1b)}
\end{aligned}$$

and

$$\frac{dh_0}{dt} = \frac{1}{\Delta^2}[4\gamma_0 - \gamma_1 - \gamma_3 - \gamma_5 - \gamma_7] \qquad \text{(A.1c)}$$

where $q_{abcd} \equiv \frac{1}{4}(q_a + q_b + q_c + q_d)$ with subscripts referring to Figure 1. At the representative 'western' boundary point $(1, j)$, the evolution equations take the forms

$$\frac{d\zeta_{1j}}{dt} = \frac{1}{6\Delta^2}[\chi_{2,j-1}(q_{1,j-1} - q_{2j}) + \chi_{2j}(q_{1,j-1} + q_{2,j-1} - q_{1,j+1} - q_{2,j+1}) + \chi_{2,j+1}(q_{2j} - q_{1,j+1})] + \frac{1}{2\Delta^2}[(q_{1j} + q_{1,j+1})(\gamma_{1j} - \gamma_{1,j+1}) + 2(q_{1j} + q_{2j})(\gamma_{1j} - \gamma_{2j}) + (q_{1j} + q_{1,j-1})(\gamma_{1j} - \gamma_{1,j-1})] + \frac{1}{\Delta}(G_{2j} - G_{1j}) + \frac{1}{2\Delta}(F_{1,j-1} - F_{1,j+1}) \tag{A.2a}$$

$$\frac{d\mu_{1j}}{dt} = \frac{1}{4\Delta^2}[(q_{1j} + q_{2j} + q_{1,j+1} + q_{2,j+1})(\gamma_{1,j+1} - \gamma_{2j}) + (q_{1j} + q_{2j} + q_{1,j-1} + q_{2,j-1})(\gamma_{2j} - \gamma_{1,j-1})] + \frac{1}{\Delta^2}\chi_{2j}(q_{1j} + q_{2j}) + \frac{1}{\Delta^2}[4\Phi_{1j} - 2\Phi_{2j} - \Phi_{1,j-1} - \Phi_{1,j+1}] + \frac{1}{\Delta}(F_{1j} + F_{2j}) + \frac{1}{2\Delta}(G_{1,j+1} - G_{1,j-1}) \tag{A.2b}$$

$$\frac{dh_{1j}}{dt} = \frac{1}{\Delta^2}[4\gamma_{1j} - 2\gamma_{2j} - \gamma_{1,j-1} - \gamma_{1,j+1}]. \tag{A.2c}$$

At the representative 'southwestern' corner point (1,1), the evolution equations take the forms

$$\frac{d\zeta_{11}}{dt} = \frac{1}{3\Delta^2}\chi_{22}(q_{21} - q_{12}) + \frac{1}{\Delta^2}[(q_{11} + q_{12})(\gamma_{11} - \gamma_{12}) + (q_{11} + q_{21})(\gamma_{11} - \gamma_{21})] + \frac{1}{\Delta}(G_{21} - G_{11}) + \frac{1}{\Delta}(F_{11} - F_{12}) \tag{A.3a}$$

$$\frac{d\mu_{11}}{dt} = \frac{1}{2\Delta^2}(q_{11} + q_{12} + q_{21} + q_{22})(\gamma_{12} - \gamma_{21}) + \frac{2}{\Delta^2}(2\Phi_{11} - \Phi_{12} - \Phi_{21}) + \frac{1}{\Delta}(F_{11} + F_{21}) + \frac{1}{\Delta}(G_{11} + G_{12}) \tag{A.3b}$$

$$\frac{dh_{11}}{dt} = \frac{2}{\Delta^2}(2\gamma_{11} - \gamma_{12} - \gamma_{21}). \tag{A.3c}$$

At the representative interior point shown in Figure 2, the diagnostic equations (2.8) and (2.11) take the forms

$$\zeta_0 = \frac{2}{\Delta^2}\left[\frac{\chi_1 - \chi_0}{h_1 + h_0} + \frac{\chi_3 - \chi_0}{h_3 + h_0} + \frac{\chi_5 - \chi_0}{h_5 + h_0} + \frac{\chi_7 - \chi_0}{h_7 + h_0}\right] + \frac{2}{\Delta^2}\left[\frac{(\gamma_3 - \gamma_1)}{(h_0 + h_1 + h_2 + h_3)} + \frac{(\gamma_5 - \gamma_3)}{(h_0 + h_3 + h_4 + h_5)} + \frac{(\gamma_7 - \gamma_5)}{(h_0 + h_5 + h_6 + h_7)} + \frac{(\gamma_1 - \gamma_7)}{(h_0 + h_7 + h_8 + h_1)}\right] \tag{A.4a}$$

$$\mu_0 = \frac{2}{\Delta^2}\left[\frac{\gamma_1-\gamma_0}{h_1+h_0}+\frac{\gamma_3-\gamma_0}{h_3+h_0}+\frac{\gamma_5-\gamma_0}{h_5+h_0}+\frac{\gamma_7-\gamma_0}{h_7+h_0}\right]$$
$$+\frac{2}{\Delta^2}\left[\frac{(\chi_1-\chi_3)}{(h_0+h_1+h_2+h_3)}+\frac{(\chi_3-\chi_5)}{(h_0+h_3+h_4+h_5)}\right.$$
$$\left.+\frac{(\chi_5-\chi_7)}{(h_0+h_5+h_6+h_7)}+\frac{(\chi_7-\chi_1)}{(h_0+h_7+h_8+h_1)}\right] \tag{A.4b}$$

$$\Phi_0 = gh_0+\frac{1}{\Delta^2}\left[\frac{(\chi_1-\chi_0)^2+(\gamma_1-\gamma_0)^2}{(h_0+h_1)^2}+\frac{(\chi_3-\chi_0)^2+(\gamma_3-\gamma_0)^2}{(h_0+h_3)^2}\right.$$
$$\left.+\frac{(\chi_5-\chi_0)^2+(\gamma_5-\gamma_0)^2}{(h_0+h_5)^2}+\frac{(\chi_7-\chi_0)^2+(\gamma_7-\gamma_0)^2}{(h_0+h_7)^2}\right]$$
$$+J_{0123}+J_{7810}+J_{5034}+J_{6705} \tag{A.4c}$$

where

$$J_{abcd} \equiv \frac{2[(\chi_c-\chi_a)(\gamma_d-\gamma_b)-(\gamma_c-\gamma_a)(\chi_d-\chi_b)]}{(h_a+h_b+h_c+h_d)^2\Delta^2}. \tag{A.4d}$$

At the representative 'western' boundary point $(1, j)$, the diagnostic equations take the forms

$$\mu_{1j} = \frac{2}{\Delta^2}\left[\frac{(\gamma_{1,j+1}-\gamma_{1j})}{(h_{1j}+h_{1,j+1})}+2\frac{(\gamma_{2j}-\gamma_{1j})}{(h_{1j}+h_{2j})}+\frac{(\gamma_{1,j-1}-\gamma_{1j})}{(h_{1j}+h_{1,j-1})}\right]$$
$$+\frac{4}{\Delta^2}\chi_{2j}\left[\frac{1}{(h_{1j}+h_{2j}+h_{1,j+1}+h_{2,j+1})}-\frac{1}{(h_{1j}+h_{2j}+h_{1,j-1}+h_{2,j-1})}\right] \tag{A.5a}$$

$$\Phi_{1j} = gh_{1j}+\frac{1}{\Delta^2}\left[\frac{(\gamma_{1,j+1}-\gamma_{1j})^2}{(h_{1j}+h_{1,j+1})^2}+2\frac{\chi_{2j}^2+(\gamma_{2j}-\gamma_{1j})^2}{(h_{1j}+h_{2j})^2}+\frac{(\gamma_{1,j-1}-\gamma_{1j})^2}{(h_{1j}+h_{1,j-1})^2}\right]$$
$$+\frac{4}{\Delta^2}\left[\frac{\chi_{2,j+1}(\gamma_{1,j+1}-\gamma_{2j})+\chi_{2j}(\gamma_{2,j+1}-\gamma_{1j})}{(h_{1j}+h_{2j}+h_{1,j+1}+h_{2,j+1})^2}\right.$$
$$\left.+\frac{\chi_{2j}(\gamma_{1j}-\gamma_{2,j-1})+\chi_{2,j-1}(\gamma_{2j}-\gamma_{1,j-1})}{(h_{1j}+h_{2j}+h_{1,j-1}+h_{2,j-1})^2}\right]. \tag{A.5b}$$

At the representative 'southwestern' corner point (1, 1), the diagnostic equations take the forms,

$$\mu_{11} = \frac{4}{\Delta^2}\left[\frac{(\gamma_{12}-\gamma_{11})}{(h_{12}+h_{11})}+\frac{(\gamma_{21}-\gamma_{11})}{(h_{21}+h_{11})}\right] \tag{A.6a}$$

$$\Phi_{11} = gh_{11}+\frac{2}{\Delta^2}\left[\frac{(\gamma_{12}-\gamma_{11})^2}{(h_{11}+h_{12})^2}+\frac{(\gamma_{21}-\gamma_{11})^2}{(h_{11}+h_{21})^2}\right]+\frac{8}{\Delta^2}\frac{\chi_{22}(\gamma_{12}-\gamma_{21})}{(h_{11}+h_{12}+h_{21}+h_{22})^2} \tag{A.6b}$$

REFERENCES

Arakawa, A. 1966. Computational design for long-term numerical integration of the equations of fluid motion: two-dimensional incompressible flow. Part I. J. Comput. Phys., *1*, 119–143.

Arakawa, A. and V. R. Lamb. 1981. A potential enstrophy and energy conserving scheme for the shallow water equations. Mon. Wea. Rev., *109*, 18–36.

Bühler, O. 1993. A nonlinear wave in rotating shallow water. Woods Hole Oceanographic Institution Technical Report WHOI-94-12, 153–159.

Dukowicz, J. K. and R. J. Greatbatch. 1999. Evolution of mean-flow Fofonoff gyres in barotropic quasigeostrophic turbulence. J. Phys. Oceanogr., 29, 1832–1852.

Durran, D. R. 1999. Numerical Methods for Wave Equations in Geophysical Fluid Dynamics, Springer, NY, 465 pp.

Gill, A. E. 1982. Atmosphere-Ocean Dynamics, Academic, NY, 662 pp.

Ketefian, G. S. and M. Z. Jacobson. 2009. A mass, energy, and potential enstrophy conserving lateral fluid-land boundary scheme for the shallow water equations. J. Comp. Phys., *228*, 1–32.

Lorenz, E. N. 1960. Energy and numerical weather prediction. Tellus, *12*, 364–373.

Miles, J. W. 1972. Kelvin waves on oceanic boundaries. J. Fluid Mech., *55*, 113–127.

Mohebalhojeh, A. R. and D. G. Dritschel. 2007. Assessing the numerical accuracy of complex spherical shallow-water flows. Mon. Wea. Rev., *135*, 3876–3894.

Press, W. H., S. A Teukolsky, W. T. Vetterling and B. P. Flannery. 1992. Numerical Recipes in Fortran, 2nd ed., Cambridge, NY, 915 pp.

Randall, D. A. 1994. Geostrophic adjustment and the finite-difference shallow-water equations. Mon. Wea. Rev., *122*, 1371–1377.

Salmon, R. 1998. Lectures on Geophysical Fluid Dynamics, Oxford, NY, 362 pp.

—— 2005. A general method for conserving quantities related to potential vorticity in numerical models. Nonlinearity, *18*, R1–16.

—— 2007. A general method for conserving energy and potential enstrophy in shallow-water models. J. Atmos. Sci., *64*, 515–531.

Salmon, R. and L. D. Talley. 1989. Generalization's of Arakawa's Jacobian. J. Comput. Phys., *83*, 247–259.

Sommer, M. and P. Nevir. 2009. A conservative scheme for the shallow-water system on a staggered geodesic grid based on a Nambu representation. Q. J. Roy. Met. Soc., *135*, 485–494.

Zeitlin, V. 2007. Nonlinear Dynamics of Rotating Shallow Water, Elsevier, Amsterdam, 391 pp.

Received: *1 August, 2009*; revised: *15 January, 2010*.